

High-resolution diffraction reveals magnetoelastic coupling and coherent phase separation in tetragonal CuMnAs

Manohar H. Karigerasi,¹ Kisung Kang,¹ Jeffrey Huang,¹ Vanessa K. Peterson,² Kirrily C. Rule,² Andrew J. Studer,² André Schleife,^{1,3} Pinshane Y. Huang,¹ and Daniel P. Shoemaker^{1,*}

¹*Department of Materials Science and Engineering and Materials Research Laboratory, University of Illinois at Urbana-Champaign, Urbana, IL 61801, USA*

²*Australian Nuclear Science and Technology Organisation, New Illawarra Road, Lucas Heights, NSW 2234, Australia*

³*National Center for Supercomputing Applications, University of Illinois at Urbana-Champaign, Urbana, IL 61801, USA*

Tetragonal CuMnAs was the first antiferromagnet where reorientation of the Néel vector was reported to occur by an inverse spin galvanic effect. A complicating factor in the formation of phase-pure tetragonal CuMnAs is the formation of an orthorhombic phase with nearly the same stoichiometry. Pure-phase tetragonal CuMnAs has been reported to require an excess of Cu to maintain a single phase in traditional solid state synthesis reactions. Here we show that subtle differences in diffraction patterns signal pervasive inhomogeneity and phase separation, even in Cu-rich Cu_{1.18}Mn_{0.82}As. From calorimetry and magnetometry measurements, we identify two transitions corresponding to the Néel temperature (T_N) and an antiferromagnet to weak ferromagnet transition in Cu_{1.18}Mn_{0.82}As and CuMn_{0.964}As_{1.036}. These transitions have clear crystallographic signatures, directly observable in the lattice parameters upon in-situ heating and cooling. The immiscibility and phase separation could arise from a spinodal decomposition that occurs at high temperatures, and the presence of a ferromagnetic transition near room temperature warrants further investigation of its effect on the electrical switching behavior.

I. INTRODUCTION

In 2016, Wadley *et al.*¹ showed that it is possible to switch Mn moments in tetragonal CuMnAs between [100] and [010] using electrical currents. Metallic antiferromagnets, such as CuMnAs and Mn₂Au, are globally centrosymmetric but locally non-centrosymmetric and the individual sublattices are related to each other by an inversion center.^{1–3} Since then, there has been a growing interest in studying the magnetic ordering in metallic antiferromagnets^{4–7} and understanding how to read and manipulate their order parameter.^{1,8–10} Unlike spin transfer torque based switching,¹¹ the fieldlike torque from the inverse spin galvanic effect does not require an adjacent ferromagnet (FM) polarizer. This provides opportunity to synthesize bulk stress-free samples that do not require a substrate for the measurements. Large single crystals are also required for studying magnetic anisotropy using inelastic neutron scattering techniques.¹² However, all attempts to grow bulk crystals of CuMnAs so far have only resulted in μm -sized grains.¹³ This is in contrast to compounds such as Fe₂As, which has the same structure type as CuMnAs and can be grown in cm-sized single crystals.¹²

Complex structural and magnetic phase behavior is crucial to understand in the Cu-Mn-As system: subtle effects from antiferromagnetic domains can be easily overwhelmed by small ferromagnetic moments, and other magnetic orderings (Mn₂As in particular) do not possess the same symmetry as ideal CuMnAs. We show here that ferromagnetic moments are intrinsic in Mn-rich CuMnAs materials. Bulk ternary compounds in the Cu-Mn-As system can be grown using traditional

solid state synthesis routes.^{14–16} However, when Cu, Mn, and As elemental powders are mixed in stoichiometric proportions, the orthorhombic polymorph of CuMnAs is stabilized.^{17–19} Typically, substituting small amounts of Mn with Cu helps in stabilizing the tetragonal phase and the crossover from the orthorhombic to tetragonal phase for Cu_{1+x}Mn_{1-x}As lies somewhere between $x = 0.06 – 0.11$.¹⁵ Near-stoichiometric tetragonal CuMnAs can also be synthesized by substituting Mn with As¹⁵ and electrical transport studies have been carried out on devices prepared from bulk samples.¹³ On the Mn-excess side of Cu_{1+x}Mn_{1-x}As, the thermodynamically stable phase changes from orthorhombic CuMnAs¹⁴ to hexagonal Cu_{0.82}Mn_{1.18}As¹⁶ to orthorhombic CuMn₃As₂¹⁴ and eventually tetragonal Mn₂As.²⁰ Cu is known to substitute up to $x = 0.1$ in Mn_{2-x}Cu_xAs.¹⁵ The crossover to tetragonal Mn₂As is intriguing since it has the same structure type as tetragonal CuMnAs. It may be possible, therefore, to also synthesize phase pure tetragonal CuMnAs with Mn excess.

The effect of increasing Cu substitution results in a decrease of the Néel temperature (T_N).¹⁵ Separately, an AFM-FM transition was observed by Uhlirova, *et al.* in near-stoichiometric samples around 315 K which was attributed to a possible MnAs impurity.¹⁵ The first manuscript on the discovery of CuMnAs also reports a Curie temperature (T_c) at 300 K.²¹ Surprisingly, the AFM-FM transition has not been reported in any of the thin-film electrical switching papers.^{1,10,22} Confirmation of the absence of a FM component in thin film transport studies is not routine, so the possibility of coupling to a polarizable moment must be investigated, and we confirm this AFM-FM transition with diffrac-

tion and calorimetry measurements here. Despite the significance of bulk CuMnAs in understanding spin orbit torques in AFM, most electrical switching studies have only used epitaxially grown thin films. While magnetometry and calorimetry measurements have been carried out for the tetragonal phase on the Cu-excess side of $\text{Cu}_{1+x}\text{Mn}_{1-x}\text{As}$,¹⁵ high resolution x-ray and neutron diffraction measurements are warranted for studying the phase stabilities and for understanding anomalies such as the low temperature ferromagnetic transition,^{15,21} unipolar magnetic anisotropies, and low anisotropic magnetoresistance values.¹³

In this article, we synthesize Cu-Mn-As samples at three different stoichiometries: Cu-rich $\text{Cu}_{1.18}\text{Mn}_{0.82}\text{As}$, Mn-rich $\text{Cu}_{0.64}\text{Mn}_{1.36}\text{As}$ and a near-stoichiometric $\text{CuMn}_{0.964}\text{As}_{1.036}$. The near-stoichiometric tetragonal $\text{CuMn}_{0.964}\text{As}_{1.036}$ composition has been reported and studied in previous papers (Uhlirova *et al.* (2019), Volny *et al.* (2020) etc.),^{13,15} so we synthesize and examine it here. Our Cu-excess $\text{Cu}_{1.18}\text{Mn}_{0.82}\text{As}$ composition lies close to the boundary between the tetragonal and orthorhombic structure ($x = 1.11$ in Uhlirova *et al.* (2019)).¹⁵ Our Mn-excess composition $\text{Cu}_{0.64}\text{Mn}_{1.36}\text{As}$ is investigated here because it is the first compound along the $\text{Cu}_x\text{Mn}_{1-x}\text{As}$ line that is Mn-rich and showed a pure tetragonal structure, without traces of orthorhombic CuMnAs. Using scanning transmission electron microscopy (STEM) imaging, synchrotron x-ray diffraction (XRD), and neutron powder diffraction (NPD) measurements, we examine complex phase separation and sample inhomogeneity in the Cu-rich and Mn-rich samples. Using calorimetry, superconducting quantum interference device (SQUID) magnetometry, synchrotron XRD and NPD measurements, we report strong magnetoelastic transitions at around 300 K and T_N in the Cu-rich and the near-stoichiometric samples. The coherent stripe order of alternating domains with different Cu/Mn ratios implies that they could be altered by thermal cycling and likely contribute to anisotropic magnetoresistance measurements.

II. METHODS

All three samples, Cu-rich $\text{Cu}_{1.18}\text{Mn}_{0.82}\text{As}$, Mn-rich $\text{Cu}_{0.64}\text{Mn}_{1.36}\text{As}$ and near-stoichiometric $\text{CuMn}_{0.964}\text{As}_{1.036}$, were synthesized using traditional solid state synthesis routes. The elemental powders of Cu (99.9% metals basis), Mn (99.98% metals basis), and As (99.9999% metals basis) were mixed in 1.18:0.82:1 ratio for the Cu-rich sample, 0.64:1.36:1 ratio in the Mn-rich sample, and in 1:0.964:1.036 ratio for the near-stoichiometric sample in an Ar-filled glovebox. The mixed powders were vacuum sealed in quartz tubes and heated to 873 K in 10 h. The samples were held at 873 K for 6 h before heating to 1248 K at 1 K/min and held for 1 h. The Cu-rich and Mn-rich samples were cooled to 1173 K at 1 K/min and held for 1 h before furnace-

cooling to room temperature. The near-stoichiometric sample was cooled slowly to 1023 K at 0.5 K/min and held for 1 h before cooling. Unlike the Cu-rich sample, mixed powders of the near-stoichiometric sample were transferred to an alumina crucible and the crucible was vacuum sealed inside a quartz tube in accordance with Uhlirova *et al.*¹⁵ The resulting ingots were black in color and lightly stuck to the tube or crucible.

Variable-temperature synchrotron XRD measurements of the Cu-rich sample were taken using a nitrogen blower at beamline 11-BM of the Advanced Photon Source in Argonne National Laboratory.²³ Powder XRD measurements for the near-stoichiometric sample were performed in a Bruker D8 Advance in reflection geometry with a Cu source. Variable-temperature neutron powder diffraction (NPD) measurements for the Cu-rich and Mn-rich samples were carried out in POWGEN beamline at Spallation Neutron Source in Oak Ridge National Laboratory.^{24,25} Additional NPD for the Cu-rich sample were collected on the Wombat instrument at the Australian Center for Neutron Scattering (ACNS).²⁶ On Wombat, data were collected in a top loading cryostat in a vanadium can with copper heating blocks and a conduction arm between them at the top and the bottom of the sample, and an aluminium heat shield placed around both blocks and the sample. The NPD measurements were carried out at 4.6167(31) Å wavelength while cooling and at 2.41 Å wavelength while heating. Data for the near-stoichiometric sample were collected on Echidna at ACNS²⁷ at 2.43872(8) Å in a vanadium can at 4 K, 400 K, and 520 K in the same top-loading cryofurnace set-up as collected on Wombat. Rietveld analyses of XRD were performed using GSAS-II software.²⁸ The magnetic structure refinement of the NPD data with help from k-SUBGROUPSMAG program²⁹ in the Bilbao Crystallographic Server was carried out in GSAS-II.²⁸ The instrumental parameters for the Echidna data were obtained from the NIST SRM La¹¹B₆ 660b data and fixed in those sample refinements. More information on the refinement approach to the XRD and NPD data is provided in supplementary.³⁰ The starting structures for CuMnAs and MnO refinements were taken from ICSD # 423230 and 9864, respectively. The space group for the CuMnAs structure used in the refinements is $P4/nmm$.

Field cooling (FC) and zero field cooling (ZFC) curves with a field of 10 kOe for the samples were measured using a brass half-tube sample holder in a Quantum Design MPMS3 vibrating sample magnetometer. Powders of the samples weighing less than 10 mg were transferred to Al pans and differential scanning calorimetry (DSC) measurements were taken using a heat-cool-heat cycle between 93 K and 673 K at 10 K/min in a TA Instruments DSC 2500.

Scanning transmission electron microscopy (STEM) images and energy dispersive X-ray spectroscopy (EDS) elemental maps were obtained at room temperature using a Thermo Fisher Themis Z STEM operated at 300 kV with 25 mrad convergence angle. Images were acquired

with approximately 50 pA probe current and EDS data with approximately 500 pA. EDS spectra were acquired over 2048×2048 probe positions. EDS elemental maps were produced using the Velox software and smoothed with a moving average filter with a width of 41 pixels.

First-principles density functional theory (DFT) simulations were performed using the Vienna *Ab-Initio* Simulation Package (VASP).^{31,32} The Brillouin zone was sampled using an $18 \times 18 \times 10$ Monkhorst-Pack³³ k -point grid. Kohn-Sham states were expanded into a plane wave basis with a kinetic-energy cutoff of 600 eV. These parameters allowed for converged calculations of the total energy within 0.6 meV per formula unit. The generalized-gradient approximation as parametrized by Perdew, Burke, and Ernzerhof³⁴ (PBE) was used to describe the exchange and correlation contribution to the DFT Hamiltonian, in combination with an on-site Coulomb interaction, described using the DFT+ U approach of Dudarev *et al.*³⁵ U_{eff} values from the literature are adopted, as discussed in detail in Sec. III B. We use a noncollinear description of magnetism including the effect of spin-orbit coupling.³⁶ Here we compare two cases: First, we relax all atomic coordinates using the DFT ground state result for the magnetic structure, which shows the $Pm'mn$ (# 59.407 in the Belov-Neronova-Smirnova (BNS) notation) magnetic space group with a magnetic moment on the Mn site only. Next, to test if there is any tendency for local moments on Cu, we impose a constrained magnetic structure with a magnetic moment of $2.77 \mu_B$ on the Mn site and $0.50 \mu_B$ on the Cu site and relax again all atomic positions.

III. RESULTS AND DISCUSSION

A. Phase separation and heterogeneity

Cu-rich $\text{Cu}_{1.18}\text{Mn}_{0.82}\text{As}$: Fig. 1(a) shows the Rietveld fit to the synchrotron XRD data taken at 298 K. For laboratory x-ray diffraction data, the fit to tetragonal CuMnAs is satisfactory, but our high resolution data in Fig. 1(a) reveals a poor fit to the 001 peak, as visible in the inset. There is pervasive peak splitting from room temperature to 450 K, as we will discuss subsequently. X-rays cannot discriminate between Cu and Mn occupancies in CuMnAs due to their close electron counts. Neutrons, on the other hand, give distinct scattering lengths for Cu and Mn (7.72 and -3.73 fm, respectively). From fits to 500 K NPD measurements in Fig. 1(b), the peak splitting is not apparent and the refined Cu:Mn stoichiometry was obtained as $1.186(3):0.814(3)$, which matches the nominal synthesis stoichiometry. In the refinement, Cu was allowed to partially occupy Mn sites and the total occupancy was constrained to be 1 at the Mn site. When Mn was also allowed to partially occupy Cu sites, the refinement yielded negligible values for Mn occupancy. This proves that, on average, excess Cu substitutes into Mn sites in $\text{Cu}_{1.18}\text{Mn}_{0.82}\text{As}$.

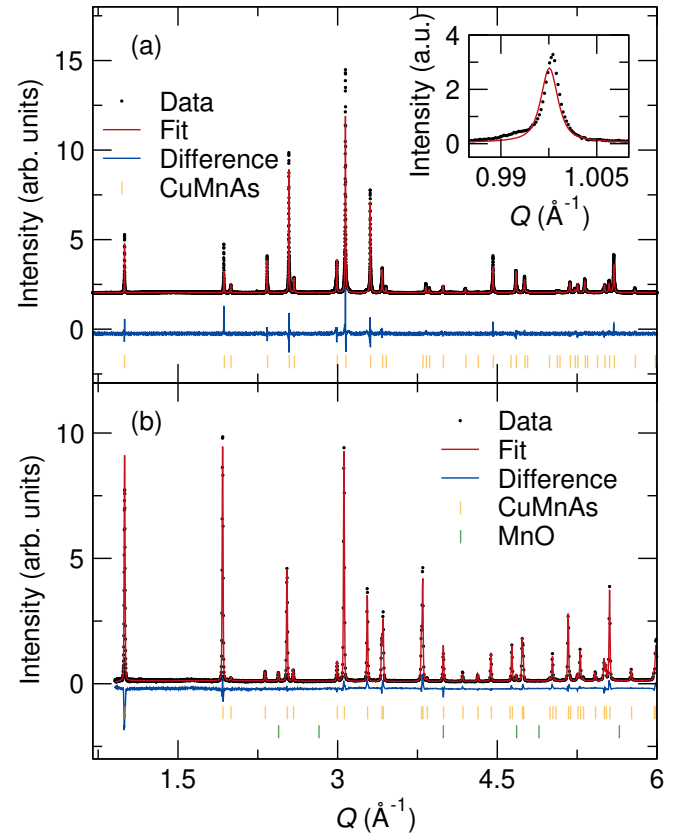


FIG. 1. Rietveld fit to 298 K synchrotron XRD data of $\text{Cu}_{1.18}\text{Mn}_{0.82}\text{As}$ is shown in (a) and the fit to 500 K POWGEN NPD (above T_N , upon heating from 300 K) data is shown in (b). Asymmetry in the low- Q peak inset (and the resulting poor fit) is evident due to the phase transition more visible in temperature-dependent measurements in Fig. 3. The material is single-phase at 500 K.

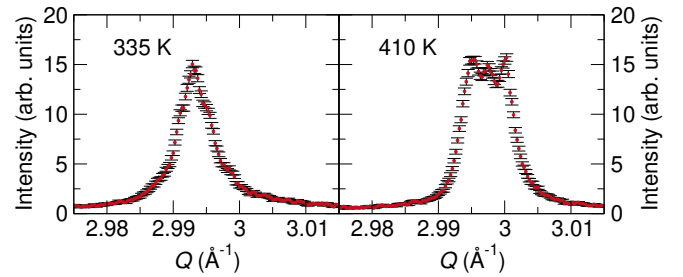


FIG. 2. The 003 synchrotron XRD peak is shown at 335 K and 410 K for the same $\text{Cu}_{1.18}\text{Mn}_{0.82}\text{As}$ sample as the temperature map in Fig. 3(a). At least three peaks are apparent at 410 K.

While there were subtle peak splittings in the synchrotron XRD data shown in Fig. 1(a), a close look at the 003 XRD peaks upon heating shows more complex and pervasive changes. The splitting of the 003 XRD peak into three peaks is shown in Fig. 2, and as a contour plot versus temperature in Fig. 3(a). We later show that the peak splitting occurs due to chemical inhomogeneity and

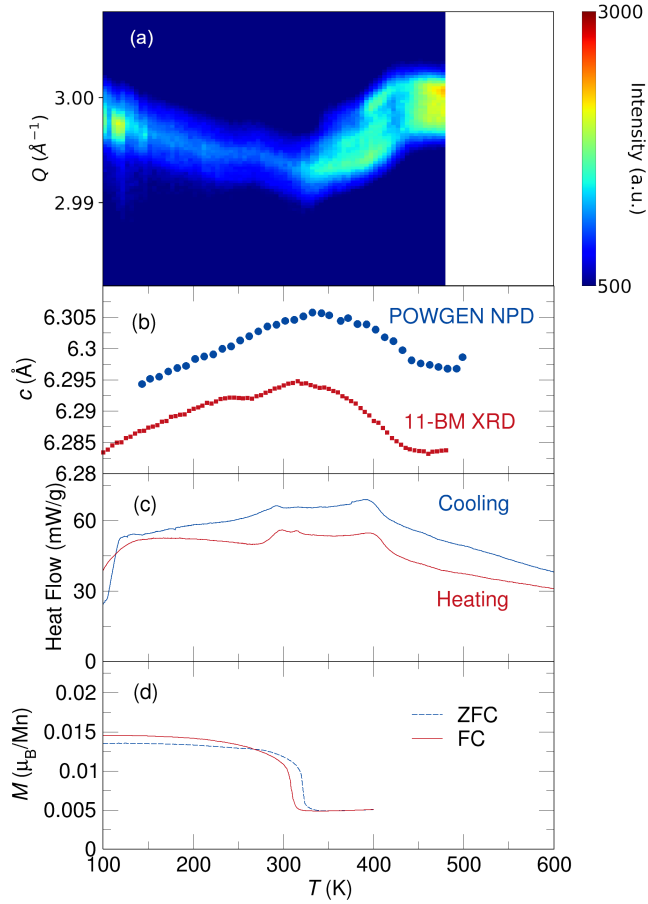


FIG. 3. For the Cu-rich sample $\text{Cu}_{1.18}\text{Mn}_{0.82}\text{As}$, the in-situ synchrotron XRD measurements (collected on heating) have sufficient resolution to observe splitting in the higher-order 003 peak, which is shown in (a). (b) shows the change in c lattice parameter across temperature as determined from a single-peak fit to the 001 reflections in synchrotron XRD and POWGEN NPD measurements. The DSC heating (inverted) and cooling curves are shown in (c) and the field cooling and zero field cooling curves are shown in (d). More than two phases are present in the intermediate temperature range from 300 to 400 K.

phase separation as evidenced in the TEM images shown in Fig. 4. The peak splitting behavior is not resolvable in the POWGEN NPD measurements. However, if an average c lattice parameter is estimated as a peak fit to the 001 reflection for all measurements, consistent trends appear from POWGEN neutron measurements and 11-BM synchrotron measurements as shown in Fig. 3(b). The discrepancy in the c lattice parameters between the two measurements can be attributed to peak shift effects such as sample displacement that is not taken into account during peak fitting. Sequential peak fits to the 001 reflection of the Wombat neutron data in Fig. S1³⁰ shows a lack of change in the slope of the c lattice parameter below 300 K.

Fig. 3(c) shows the results of DSC measurements for

the $\text{Cu}_{1.18}\text{Mn}_{0.82}\text{As}$ sample. We observe two kinks at around 300 K and 420 K respectively. The transition at 420 K corresponds to the T_N of the sample. This is also confirmed from studies by Uhlirova *et al.*¹⁵ where increasing the Cu substitution at Mn sites decreases the T_N considerably from its maximum value of around 520 K. The transition at 300 K has a clear signature in magnetic susceptibility shown in Fig. 3(d). There is an increase in the net moment below 300 K indicating a possible transition from an AFM to a weak FM phase. As mentioned earlier, the ferromagnetic transition has been reported in previous studies,^{15,21} although it was tentatively attributed to the presence of a possible MnAs impurity. This explanation is unlikely since we do not observe any MnAs impurity in the synchrotron XRD data of the Cu-rich sample as shown in Fig. 1(a), and the presence of a phase transition in the majority CuMnAs phase is clear from in-situ diffraction data and calorimetry in Fig. 3(a,b,c). Similar transitions are also observed in the DSC and SQUID measurements of the near-stoichiometric sample, as we discuss subsequently. Such changes in lattice parameters around T_N are not observed in Fe_2As , which has the same structure type as CuMnAs, as shown in Fig. S2.³⁰

Since diffraction measurements did not permit refinement of Cu/Mn occupancies in both phases simultaneously, a focused ion beam (FIB) cross-section of the Cu-rich $\text{Cu}_{1.18}\text{Mn}_{0.82}\text{As}$ sample was examined via STEM. Fig. 4(a) shows the microstructure and STEM-EDS elemental mapping of a polished surface in the Cu-rich sample. Aligned stripes of two distinct phases are clearly present in the annular dark field (ADF) STEM image. EDS Elemental mapping could accurately measure the Cu content due to the background from the Cu grid, but the Mn:As ratios in the two samples were measured to be approximately 0.2 and 0.8 in the bright and dark regions, respectively. This is likely an underestimation since the nominal and neutron-refined Mn:As ratio is 0.82, but it is clear that the chemical separation is pervasive. More ADF-STEM images of the Cu-rich $\text{Cu}_{1.18}\text{Mn}_{0.82}\text{As}$ sample are shown in Fig. S3.³⁰ Fig. S3(a)³⁰ shows heterogeneity even outside the region containing the tweed-like patterns shown in Fig. 4(a).

The interdependence of phase separation and magnetism hint at strong coupling, reminiscent of martensitic shape memory alloys. This type of phase separation of topologically connected phases with subtle chemical phase separation has also been observed in intermetallics and perovskite and spinel oxides.^{37–39} Ni and Khachaturyan presented a detailed model showing how a pseudospinodal transformation from a high-symmetry phase to lower-symmetry components can result in tweed-like structures seen in metal alloys and oxide ceramics.⁴⁰ The precise reason for this phase separation is not known. The metallicity and lack of local moments on Cu in CuMnAs argues against a Jahn-Teller-driven effect, further evidenced by the fact that the phase separation seems to disappear upon cooling below 300 K (see Fig. 3(a,b)). Rather, the onset of magnetic ordering must drive per-

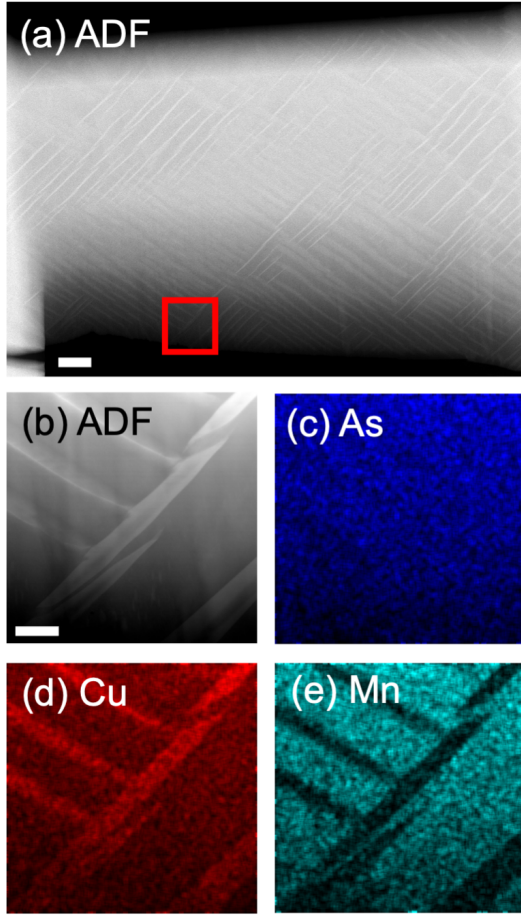


FIG. 4. For the Cu-rich $\text{Cu}_{1.18}\text{Mn}_{0.82}\text{As}$ sample, STEM micrographs of a FIB liftout reveal a tweed-like pattern in ADF imaging. The boxed area is shown in panels (b-e) for ADF, As, Cu, and Mn EDS maps. Scale bars are 500 nm in (a) and 100 nm in (b-e).

vasive lattice distortion that merits further investigation into magnetostrictive effects in Cu_2Sb -type structures, including CuMnAs .

Mn-rich $\text{Cu}_{0.64}\text{Mn}_{1.36}\text{As}$: Similar phase separation is observed in the Mn-rich composition, even at 500 K as observed by a clear splitting of the 101 peak in NPD data shown in Fig. 5. At 300 K, NPD data in Fig. 6 do not show split peaks and the material is apparently a single structural phase. This phase separation behavior may mimic the appearance of the Cu-rich composition, with the multiple-phase region in the Mn-rich sample (with more magnetic moment) shifted to higher temperatures than the Cu-rich compositions. Regardless of the lack of splitting of structural peaks at room temperature, the magnetic peak contributions in NPD patterns cannot be fit with a single k -vector: the presence of magnetic peaks corresponding to both $k = 0$ and $k = [00\frac{1}{2}]$ ordering at 300 K in Fig. 6 reveals the existence of both the established tetragonal CuMnAs $k = 0$ magnetic structure (alternating left/right moments along the c-axis) and an

Mn_2As -like $k = [00\frac{1}{2}]$ magnetic ordering. This apparent coexistence may appear due to subtle variations in local Cu/Mn concentrations, as has been seen before in two-dimensional magnetic materials that are apparently structurally phase-pure.⁴¹

Near-stoichiometric $\text{CuMn}_{0.964}\text{As}_{1.036}$: In case of the near-stoichiometric composition, good fits to room temperature synchrotron XRD and 520 K NPD measurements were obtained by fixing the Cu and Mn occupancies to be stoichiometric, as seen in Fig. 7. While some anti-site mixing of Cu and Mn is possible, there was no indication of peak splitting in the 300 K and 520 K data. However, DSC and magnetic susceptibility measurements in Fig. S4³⁰ show that two transitions indeed exist within this temperature range, at 315 and 490 K. Therefore, even the near-stoichiometric sample without Cu/Mn excess or mixing likely shows the same phase separation over a similar temperature range.

The T_N of the near-stoichiometric sample was observed to be around 490 K and the AFM-FM transformation was confirmed at 315 K which is consistent with the values reported in Uhlirova *et al.*¹⁵

B. Magnetic structure confirmation and magnetoelastic effects

A structurally-forbidden 100 magnetic peak appears at $Q = 1.65 \text{ \AA}^{-1}$ upon cooling Cu-rich $\text{Cu}_{1.18}\text{Mn}_{0.82}\text{As}$ and near-stoichiometric $\text{CuMn}_{0.964}\text{As}_{1.036}$ below T_N . This peak is most visible in the ECHIDNA NPD data at 4 K as shown for near-stoichiometric $\text{CuMn}_{0.964}\text{As}_{1.036}$ in Fig. S5³⁰ and POWGEN 300 K NPD data for $\text{Cu}_{1.18}\text{Mn}_{0.82}\text{As}$ in Fig. S6.³⁰ This corresponds to the expected $k = 0$ magnetic ordering vector. With $P4/nmm$ as the parent space group and a $k = 0$ propagation vector, there are 12 k -maximal space groups, of which 4 are in the orthorhombic crystal system as shown in Table S1.³⁰ None of the 8 magnetic subgroups in the tetragonal crystal system allow Mn moment components in the ab plane. Of the 4 k -maximal magnetic subgroups in the orthorhombic crystal system, Mn moments are ordered ferromagnetically in two of them. Of the remaining two models, a slightly better fit is obtained for the model with a $Pm'mn$ (#59.407) magnetic space group (MSG) shown in Fig. S5³⁰ which is also reported in a previous study of CuMnAs films.^{5,30} The refined magnetic moment on Mn is $3.73(3) \mu_B$.

The small uncompensated moment that arises in the Cu-rich sample at around 300 K and at 315 K in the near-stoichiometric sample requires further investigation. It is clearly an intrinsic effect since it is accompanied by a change in the lattice parameters (Fig. 3(b)). The Rietveld fit to the NPD data of the near-stoichiometric sample at 4 K using $Pm'mn$ MSG is shown in Fig. S5.³⁰ The fit is satisfactory and there is no significant improvement of fit using any of the magnetic subgroups of $Pm'mn$. We assume that the small moment arises from a canting of spins at a weak-ferromagnetic transition, which cannot

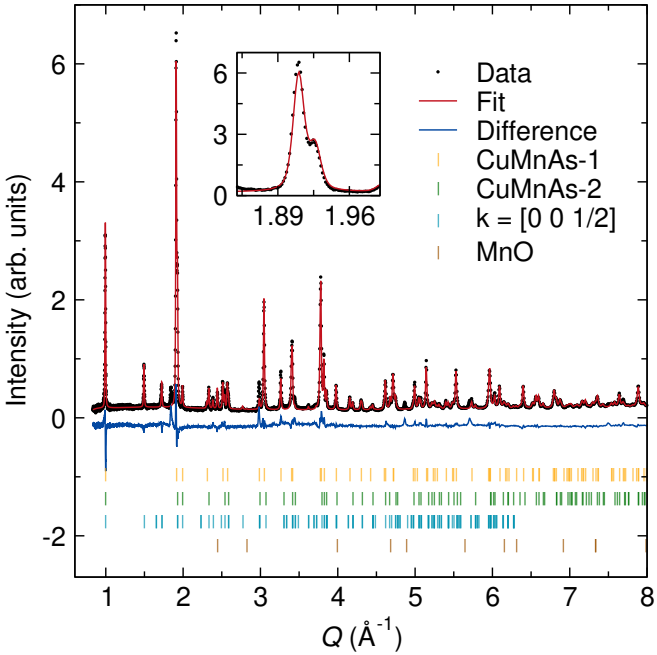


FIG. 5. Rietveld fit to the POWGEN NPD data of the Mn-rich sample $\text{Cu}_{0.64}\text{Mn}_{1.36}\text{As}$ at 500 K shows the presence of two closely-related tetragonal CuMnAs phases. The inset shows the split 101 peak that indicates a clear phase separation. One of the phases displays a Mn_2As -like $k = [00\frac{1}{2}]$ magnetic peak (as opposed to the $k = 0$ magnetic structure of near-stoichiometric CuMnAs). The peak at $Q = 1.9 \text{ \AA}$ could not be assigned, and appeared irreversibly upon initial heating.

be resolved from NPD measurements. Single-crystal susceptibility and neutron diffraction measurements could be performed if the factors affecting phase separation and crystal growth in CuMnAs can be controlled.

We use density functional theory (DFT) to describe the ground state lattice and magnetic structure of tetragonal CuMnAs. Previous studies typically use a Hubbard correction within the DFT+ U method^{42,43} to investigate tetragonal CuMnAs, using an on-site Coulomb term U and site exchange term J . Here a simplified approach is used with an effective on-site Coulomb interaction $U_{\text{eff}} = U - J$ for which values of 1.7 eV,⁴⁴ 1.92 eV,⁴⁵ 3.0 eV,⁴⁶ and 4.1 eV⁴ were reported. Here we wish to examine how the magnetic ordering and moment magnitude affects the lattice, and whether there is any tendency for local moments on Cu atoms, for different values of U_{eff} .

With increasing U_{eff} , the ratio of the lattice parameters c/a decreases from 1.742 to 1.605. The room-temperature experimental c/a ratios for the three compositions in our study span a much narrower range between 1.665 and 1.700. The calculated magnetic moment on Mn sites increases with U_{eff} , increasing from $3.412 \mu_B$ to $4.462 \mu_B$ (see Fig. 9(a)). Taking the value of c/a for the near-stoichiometric $\text{CuMn}_{0.964}\text{As}_{1.036}$ sample to prescribe U_{eff} would correspond to a calculated Mn magnetic

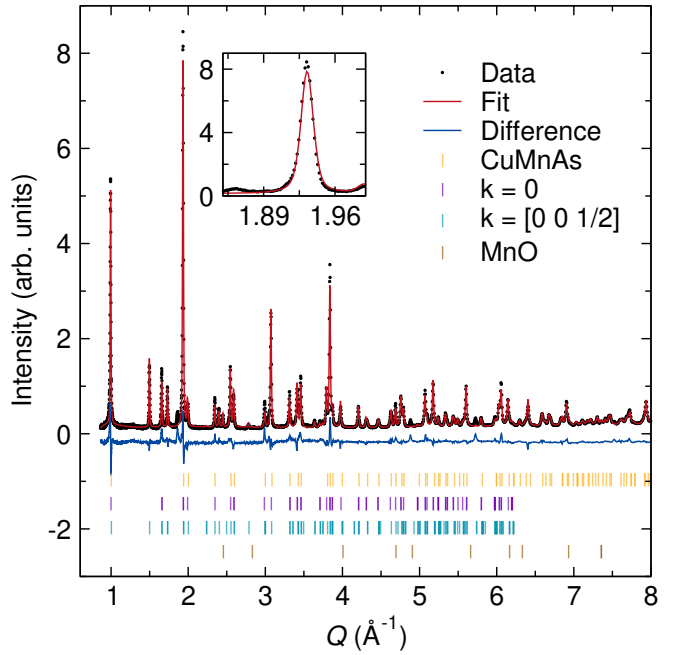


FIG. 6. Rietveld fit to the POWGEN NPD data of the Mn-rich $\text{Cu}_{0.64}\text{Mn}_{1.36}\text{As}$ sample at 300 K. The inset figure shows that unlike at 500 K, the 101 peaks does not show splitting, so there is no evidence for phase separation from structural peaks alone. However, magnetic peaks are present for both the $k = 0$ (CuMnAs-like) and $k = 00\frac{1}{2}$ (Mn_2As -like) magnetic ordering.

moment of $4.0 \mu_B$, which is in rough agreement with the refined value of $3.73(3) \mu_B$ at 4 K.

The U_{eff} -dependence of c/a and Mn magnetic moment in Fig. 9(a) show opposing trends, indicating that increased Mn magnetic moments (or increasing exchange interactions between these sites, as embodied in U_{eff}) within the ab planes may lead to a flattening of the cell, as c decreases and a increases. Magnetic interactions also must contribute to the lattice parameters observed across the compositions series, where the room-temperature in-plane a decreases with increasing Mn content across the entire compositional range, seen in Fig. 8. However, the c axis parameters at room temperature exhibit a maximum around the equiatomic CuMnAs composition. Deviating from this stoichiometry leads to regions where strong Mn exchange interactions are unsatisfied (Cu-rich) or interact with additional Mn in the nearest-neighbor plane (Mn-rich). The pervasive phase separations in these systems may be driven by nanometer-scale domains where the local magnetic ordering leads to $k = 0$ or $k = 00\frac{1}{2}$ -type ordering (as an example), which each have distinct magnetostrictive distortions to differing c/a ratios around T_N . Controlling the formation of these domains and their sizes will require investigation of high-temperature processing, where the solidus behavior and tendency to form orthorhombic CuMnAs is still unknown. The strong compositional dependence of the

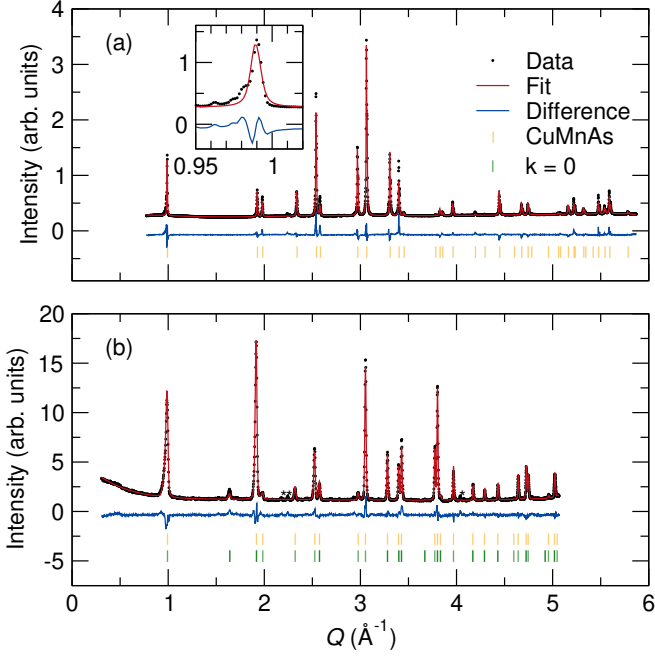


FIG. 7. Rietveld fits for the near-stoichiometric sample $\text{CuMn}_{0.964}\text{As}_{1.036}$ to the room temperature XRD data in (a) roughly fit the data, but some small amount of inhomogeneity is evident in the 001 peak, magnified in the inset. This asymmetry is not evident in the high-temperature 520 K Echidna NPD data in (b). In (b), the peak at around $Q = 1.65 \text{ \AA}^{-1}$ is a magnetic peak and the small peaks at around $Q = 2.25 \text{ \AA}^{-1}$ and 4.1 \AA^{-1} (marked by *) are impurity peaks of unknown origin.

stripes in Fig. 4 further indicate that Cu and Mn species may be mobile at the Néel temperature and weak ferromagnetic transition temperatures in CuMnAs.

Finally, DFT simulations of the ground-state magnetic structure of tetragonal CuMnAs do not show significant magnetic moments on Cu atoms, regardless of the on-site Coulomb interaction values studied here. In addition, our simulations show that the magnetic structure with non-negligible Cu magnetic moments in the constrained magnetic configurations is energetically unfavorable, regardless of the U_{eff} values studied here (see Fig. 9(b)). We also found that, in the ground state structure, the magnetization density is centrally distributed near Mn atoms and there is no population of magnetization density near Cu atoms (see Fig. S7³⁰). Based on Bader charge analysis,⁴⁸ the charge on Cu atoms is close to neutral (+0.1) which is far from the $3d^9 \text{ Cu}^{2+}$ state observed in cuprates,⁴⁹ and CuMnAs only hosts local moments on Mn. Lastly, we have implemented a total energy comparison among different types of magnetic structures from DFT simulations. The refined collinear antiferromagnetic structure has the lowest total energy among three antiferromagnetic structures and one ferromagnetic structure, confirming the agreement between the experiment and DFT for the ground state magnetic

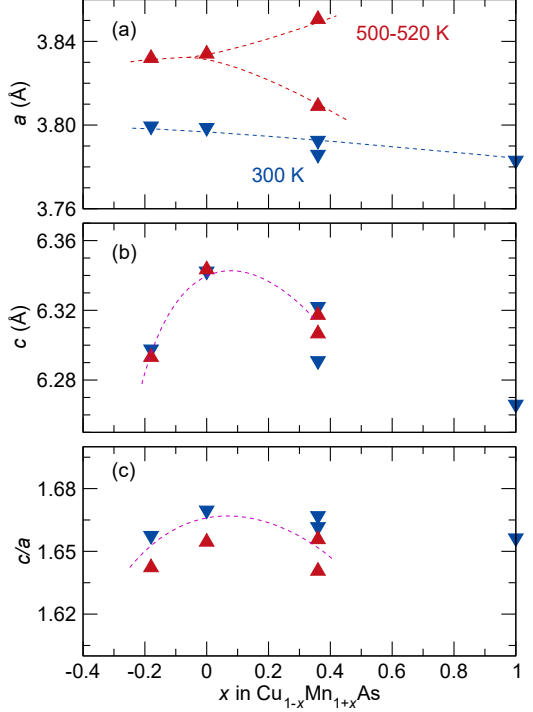


FIG. 8. The lattice parameters across various compositions obtained using NPD refinements to $T = 300$ and 500 K data. $T = 300$ K data for the Cu-excess and the near-stoichiometric sample are taken from x-ray diffraction measurements. Compositions are nominal. Values for Mn_2As are from Nuss, et al.⁴⁷ It is clear in (a) that an opposing trend in composition versus a appears above and below T_N , but this trend must be broken as x increases toward Mn_2As , and the $\text{Cu}_{0.64}\text{Mn}_{1.36}\text{As}$ composition has separated into two phases. In (b), the relative splittings in c are less variable with temperature but exhibit a maximum around the equiatomic CuMnAs composition. The c/a ratios in (c) are dominated by the trends in c . The dashed lines are used as a guide for observing trends.

configuration (see Fig. S8³⁰). A remaining question is whether magnetic ordering drives the phase separation or vice versa. Computational insight on this point may be challenging since the lattice response to compositional change is much stronger than the response to crossing T_N (Fig. 8), yet phase separation into multiple compositions is pervasive in the Cu-Mn-As system.

IV. CONCLUSIONS

The complex interplay between local stoichiometry, competing magnetically-ordered states, and magnetoelastically-driven phase separation must be considered when analyzing the results of any magnetic domain-related spintronic application in CuMnAs, whether in the bulk or in thin films, where substrate strain adds a further consideration. Pervasive phase separation is observed in three samples, Cu-rich $\text{Cu}_{1.18}\text{Mn}_{0.82}\text{As}$, Mn-rich $\text{Cu}_{0.64}\text{Mn}_{1.36}\text{As}$ and

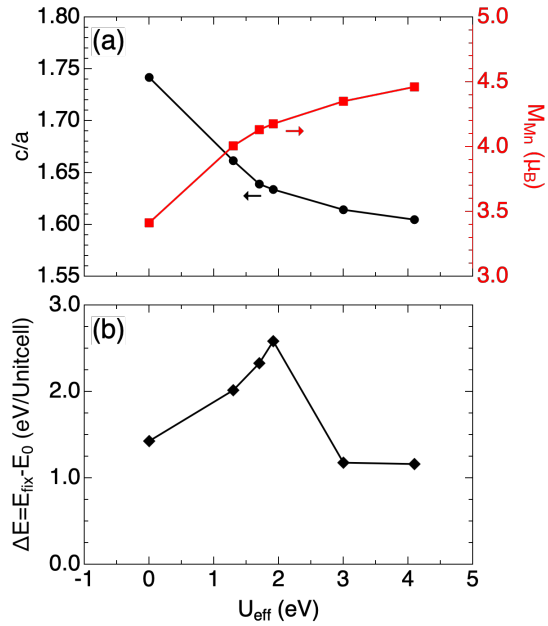


FIG. 9. (a) The lattice parameter ratio (c/a , black circles) and the magnitude of the magnetic moment at Mn atom (M_{Mn} , red squares), and (b) the energy difference between the ground state and the constrained magnetic structure with a magnetic moment at Cu atom (ΔE , black diamond) as a function of the effective on-site Coulomb interaction U_{eff} value in DFT calculations. The lines through the points are guides to the eye.

$\text{CuMn}_{0.964}\text{As}_{1.036}$ which is near-stoichiometric. Diffraction, magnetometry, and calorimetry measurements all point to the presence of two intrinsic magnetic transitions corresponding to T_N and an AFM to weak ferromagnetic transition. Lattice constants extracted from synchrotron XRD and NPD data indicate a coupling between the structural and magnetic order. A clear trend

can be drawn in the predicted c/a ratio as affected by U_{eff} , which implies that the phase separation likely arises from disordered regions of Cu or Mn clustering that are rearranged at the magnetic ordering temperatures. A clear understanding of the high-temperature behavior of these phases will aid the synthesis of single-crystal or single-phase materials, and the full picture of the phase equilibria across the Cu/Mn ratios and immiscibility behavior. Any time there is a study on the Néel order spin orbit torque with tetragonal Cu-Mn-As, we have to consider the effect of a Mn_2As based magnetic ordering as well. In same cases, such as in $\text{Cu}_{0.64}\text{Mn}_{1.36}\text{As}$, this phase is magnetic. The weak FM transition in these materials could provide an opportunity to image magnetic domains.

ACKNOWLEDGMENTS

This work was undertaken as part of the Illinois Materials Research Science and Engineering Center, supported by the National Science Foundation MRSEC program under NSF Award No. DMR-1720633. The characterization was carried out in part in the Materials Research Laboratory Central Research Facilities, University of Illinois. This research used resources of the Spallation Neutron Source, a DOE Office of Science User Facility operated by Oak Ridge National Laboratory, and the Advanced Photon Source, a DOE Office of Science User Facility operated for the DOE Office of Science by Argonne National Laboratory under Contract No. DEAC02-06CH11357. The NPD measurements in Wombat and Echidna beamlines were carried out under the proposals number DB8036 and MI1931, respectively. We thank Matthias Frontzek for assistance with NPD collection in POWGEN beamline at the Spallation Neutron Source. This work made use of the Illinois Campus Cluster, a computing resource that is operated by the Illinois Campus Cluster Program (ICCP) in conjunction with the National Center for Supercomputing Applications (NCSA) and which is supported by funds from the University of Illinois at Urbana-Champaign.

* dpschoema@illinois.edu

- ¹ P. Wadley, B. Howells, J. Zelezny, C. Andrews, V. Hills, R. P. Campion, V. Novak, K. Olejnik, F. Maccherozzi, S. S. Dhesi, S. Y. Martin, T. Wagner, J. Wunderlich, F. Freimuth, Y. Mokrousov, J. Kunes, J. S. Chauhan, M. J. Grzybowski, A. W. Rushforth, K. W. Edmonds, B. L. Gallagher, and T. Jungwirth, *Science* **351**, 587 (2016).
- ² J. Železný, H. Gao, K. Výborný, J. Zemen, J. Mašek, A. Manchon, J. Wunderlich, J. Sinova, and T. Jungwirth, *Phys. Rev. Lett.* **113**, 1 (2014).
- ³ J. Železný, H. Gao, A. Manchon, F. Freimuth, Y. Mokrousov, J. Zemen, J. Mašek, J. Sinova, and T. Jungwirth, *Phys. Rev. B* **95**, 014403 (2017).
- ⁴ P. Wadley, V. Novák, R. P. Campion, C. Rinaldi, X. Martí, H. Reichlová, J. Zelezny, J. Gazquez, M. A. Roldan, M. Varela, D. Khalyavin, S. Langridge, D. Kriegner, F. Máca, J. Masek, R. Bertacco, V. Holý, A. W. Rushforth, K. W. Edmonds, B. L. Gallagher, C. T. Foxon, J. Wunderlich, and T. Jungwirth, *Nat. Commun.* **4**, 2322 (2013).
- ⁵ P. Wadley, V. Hills, M. R. Shahedkhah, K. W. Edmonds, R. P. Campion, V. Novák, B. Ouladdiaf, D. Khalyavin, S. Langridge, V. Saidl, P. Nemec, A. W. Rushforth, B. L. Gallagher, S. S. Dhesi, F. MacCherozzi, J. Železný, and T. Jungwirth, *Sci. Rep.* **5**, 17079 (2015).
- ⁶ V. Hills, P. Wadley, R. P. Campion, V. Novak, R. Beardsley, K. W. Edmonds, B. L. Gallagher, B. Ouladdiaf, and T. Jungwirth, *J. Appl. Phys.* **117**, 172608 (2015).
- ⁷ V. Saidl, P. Nemec, P. Wadley, V. Hills, R. P. Campion, V. Novák, K. W. Edmonds, F. MacCherozzi, S. S. Dhesi, B. L. Gallagher, F. Trojánek, J. Kunes, J. Železný, P. Malý,

- and T. Jungwirth, Nat. Photonics **11**, 91 (2017).
- ⁸ M. J. Grzybowski, P. Wadley, K. W. Edmonds, R. Beardley, V. Hills, R. P. Campion, B. L. Gallagher, J. S. Chauhan, V. Novak, T. Jungwirth, F. Maccherozzi, and S. S. Dhesi, Phys. Rev. Lett. **118**, 057701 (2017).
 - ⁹ P. Wadley, S. Reimers, M. J. Grzybowski, C. Andrews, M. Wang, J. S. Chauhan, B. L. Gallagher, R. P. Campion, K. W. Edmonds, S. S. Dhesi, F. Maccherozzi, V. Novak, J. Wunderlich, and T. Jungwirth, Nat. Nanotechnol. **13**, 362 (2018).
 - ¹⁰ T. Matalla-Wagner, M. F. Rath, D. Graulich, J. M. Schmalhorst, G. Reiss, and M. Meinert, Phys. Rev. Appl. **12**, 064003 (2019).
 - ¹¹ H. V. Gomonay and V. M. Loktev, Phys. Rev. B **81**, 144427 (2010).
 - ¹² M. H. Karigerasi, K. Kang, G. E. Granroth, A. Banerjee, A. Schleife, and D. P. Shoemaker, Phys. Rev. Mater. **4**, 114416 (2020).
 - ¹³ J. Volny, D. Wagenknecht, J. Zelezny, P. Harcuba, E. Duverger-Nedellec, R. H. Colman, J. Kudrnovsky, I. Turek, K. Uhlírova, and K. Vyborny, Phys. Rev. Mater. **4**, 064403 (2020).
 - ¹⁴ K. Uhlírova, R. Tarasenko, F. J. Martinez-Casado, B. Vondrackova, and Z. Matej, J. Alloy Compd. **650**, 224 (2015).
 - ¹⁵ K. Uhlírova, E. Duverger-Nedellec, R. H. Colman, J. Volny, B. Vondrackova, and K. Carva, J. Alloy Compd. **771**, 680 (2019).
 - ¹⁶ M. H. Karigerasi, K. Kang, A. Ramanathan, D. L. Gray, M. D. Frontzek, H. Cao, A. Schleife, and D. P. Shoemaker, Phys. Rev. Mater. **3**, 111402 (2019).
 - ¹⁷ F. Máca, J. Mašek, O. Stelmakhovych, X. Martí, H. Reichenlová, K. Uhlírová, P. Beran, P. Wadley, V. Novák, and T. Jungwirth, J. Magn. Magn. Mater. **324**, 1606 (2012).
 - ¹⁸ E. Emmanouilidou, H. Cao, P. Tang, X. Gui, C. Hu, B. Shen, J. Wu, S.-C. Zhang, W. Xie, and N. Ni, Phys. Rev. B **96**, 224405 (2017).
 - ¹⁹ E. Emmanouilidou, J. Liu, D. Graf, H. Cao, and N. Ni, J. Magn. Magn. Mater. **469**, 570 (2019).
 - ²⁰ A. E. Austin, E. Adelson, and W. H. Cloud, J. Appl. Phys. **33**, 1356 (1962).
 - ²¹ A. N. Nateprov, V. C. Kravtsov, V. Fritsch, and H. von Löheynes, Surf. Eng. Appl. Elect. **47**, 540 (2011).
 - ²² M. Meinert, D. Graulich, and T. Matalla-wagner, Phys. Rev. Appl. **9**, 64040 (2018).
 - ²³ J. Wang, B. H. Toby, P. L. Lee, L. Ribaud, S. M. Antao, C. Kurtz, M. Ramanathan, R. B. Von Dreele, and M. A. Beno, Rev. Sci. Instrum. **79**, 085105 (2008).
 - ²⁴ A. Huq, M. Kirkham, P. F. Peterson, J. P. Hodges, P. S. Whitfield, K. Page, T. Hugle, E. B. Iverson, A. Parizzi, and G. Rennich, J. Appl. Crystallogr. **52**, 1189 (2019).
 - ²⁵ T. E. Mason, D. Abernathy, I. Anderson, J. Ankner, T. Egami, G. Ehlers, A. Ekkebus, G. Granroth, M. Hagen, K. Herwig, J. Hodges, C. Hoffmann, C. Horak, L. Horton, F. Klose, J. Larese, A. Mesecar, D. Myles, J. Neufeind, M. Ohl, C. Tulk, X.-L. Wang, and J. Zhao, Physica B **385**, 955 (2006).
 - ²⁶ A. J. Studer, M. E. Hagen, and T. J. Noakes, Physica B **385-386**, 1013 (2006).
 - ²⁷ M. Avdeev and J. R. Hester, J. Appl. Crystallogr. **51**, 1597 (2018).
 - ²⁸ B. H. Toby and R. B. Von Dreele, J. Appl. Crystallogr. **46**, 544 (2013).
 - ²⁹ J. Perez-Mato, S. Gallego, E. Tasçi, L. Elcoro, G. de la Flor, and M. Aroyo, Ann. Rev. Mater. Res. **45**, 217 (2015).
 - ³⁰ Supplementary Material available online.
 - ³¹ G. Kresse and J. Furthmüller, Phys. Rev. B **54**, 11169 (1996).
 - ³² G. Kresse and D. Joubert, Phys. Rev. B **59**, 1758 (1999).
 - ³³ H. J. Monkhorst and J. D. Pack, Phys. Rev. B **13**, 5188 (1976).
 - ³⁴ J. P. Perdew, K. Burke, and M. Ernzerhof, Phys. Rev. Lett. **77**, 3865 (1996).
 - ³⁵ S. L. Dudarev, G. A. Botton, S. Y. Savrasov, C. J. Humphreys, and A. P. Sutton, Phys. Rev. B **57**, 1505 (1998).
 - ³⁶ S. Steiner, S. Khmelevskyi, M. Marsmann, and G. Kresse, Phys. Rev. B **93**, 224425 (2016).
 - ³⁷ Y. Le Bouar, A. Loiseau, and A. Khachaturyan, Acta Mater. **46**, 2777 (1998).
 - ³⁸ B. S. Guiton and P. K. Davies, Nat. Mater. **6**, 586 (2007).
 - ³⁹ S. Park, Y. Horibe, T. Asada, L. S. Wielunski, N. Lee, P. L. Bonanno, S. M. O'Malley, A. A. Sirenko, A. Kazimirov, M. Tanimura, T. Gustafsson, and S.-W. Cheong, Nano Lett. **8**, 720 (2008).
 - ⁴⁰ Y. Ni and A. G. Khachaturyan, Nat. Mater. **8**, 410 (2009).
 - ⁴¹ A. Bhutani, J. L. Zuo, R. D. McAuliffe, C. R. Dela Cruz, and D. P. Shoemaker, Phys. Rev. Mater. **4**, 34411 (2020).
 - ⁴² V. I. Anisimov, J. Zaanen, and O. K. Andersen, Phys. Rev. B **44**, 943 (1991).
 - ⁴³ V. I. Anisimov, F. Aryasetiawan, and A. I. Lichtenstein, J. Phys. Condens. Matter **9**, 767 (1997).
 - ⁴⁴ M. Veis, J. Minár, G. Steciuk, L. Palatinus, C. Rinaldi, M. Cantoni, D. Kriegner, K. K. Tikuišis, J. Hamrle, M. Zahradník, R. Antoš, J. Železný, L. Šmejkal, X. Martí, P. Wadley, R. P. Campion, C. Frontera, K. Uhlírová, T. Duchoň, P. Kužel, V. Novák, T. Jungwirth, and K. Výborný, Phys. Rev. B **97**, 125109 (2018).
 - ⁴⁵ I. A. Zhuravlev, A. Adhikari, and K. D. Belashchenko, Appl. Phys. Lett. **113**, 162404 (2018).
 - ⁴⁶ S.-G. Xu, Z.-J. Chen, X.-B. Chen, Y.-J. Zhao, H. Xu, and X. Zhang, Phys. Rev. B **102**, 125123 (2020).
 - ⁴⁷ J. Nuss, U. Wedig, and M. Jansen, Z. Kristallogr. **221**, 554 (2006).
 - ⁴⁸ W. Tang, E. Sanville, and G. Henkelman, J. Phys. Condens. Matter **21**, 084204 (2009).
 - ⁴⁹ G. M. De Luca, G. Ghiringhelli, M. Moretti Sala, S. Di Matteo, M. W. Haverkort, H. Berger, V. Bisogni, J. C. Cezar, N. B. Brookes, and M. Salluzzo, Phys. Rev. B **82**, 214504 (2010).

High-resolution diffraction reveals magnetoelastic coupling and coherent phase separation in tetragonal CuMnAs

Supplementary Material

Manohar H. Karigerasi, Kisung Kang, Jeffrey Huang, Vanessa K. Peterson, Kirrily C. Rule, Andrew J. Studer, André Schleife, Pinshane Y. Huang, Daniel P. Shoemaker

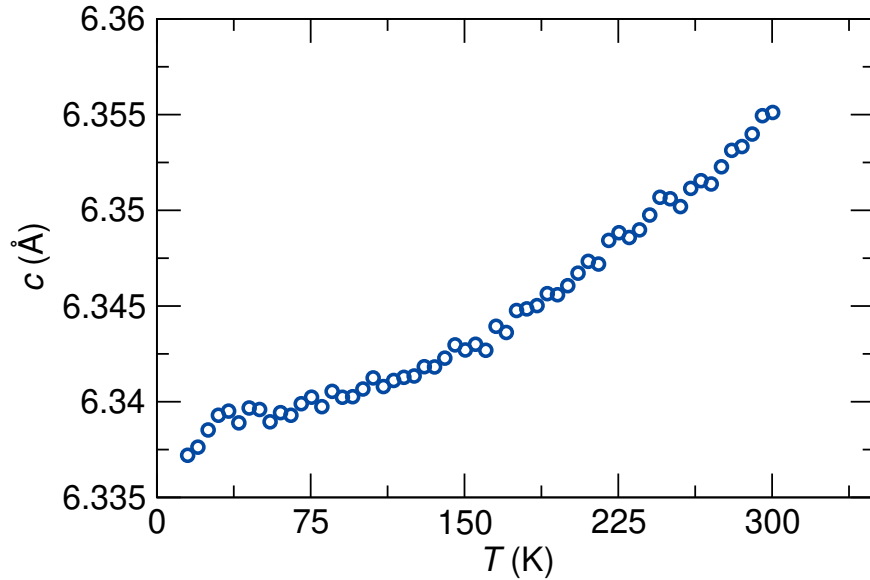


Figure 1: c lattice parameter as a function of temperature of $\text{Cu}_{1.18}\text{Mn}_{0.82}\text{As}$ extracted from a sequential peak fitting to the 001 peak in the Wombat NPD data. The values do not incorporate shifts due to sample displacements or other instrumental parameters.

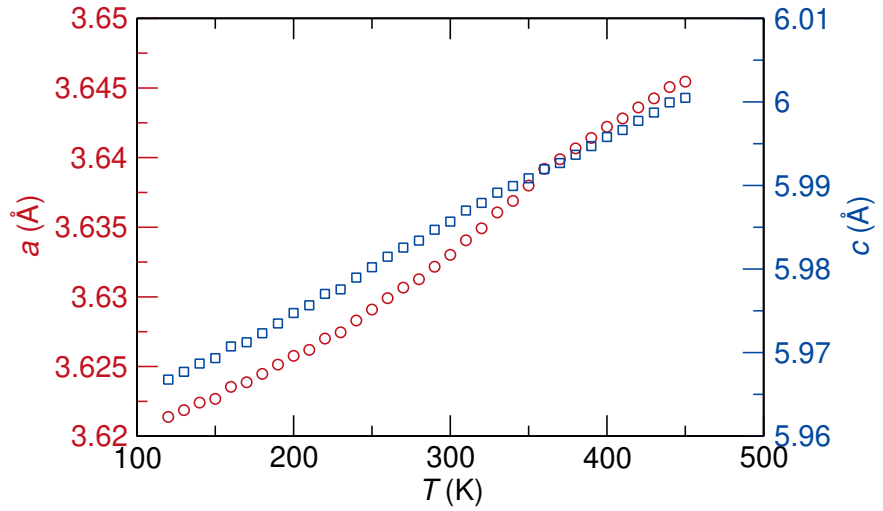


Figure 2: a and c lattice parameters of Fe_2As across a range of temperatures obtained from Rietveld refinement of synchrotron XRD data. More information on the synthesis and XRD measurements of Fe_2As can be found in Karigerasi *et al.* (2020).

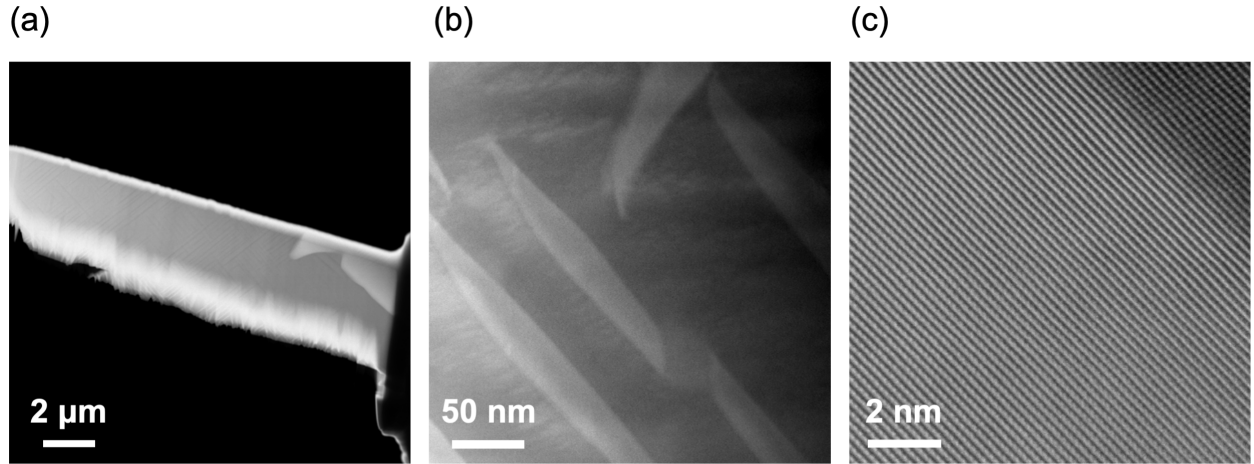


Figure 3: ADF-STEM images of the Cu-rich sample at different magnifications. (a) shows the zoomed-out view of the TEM sample where we can see two different regions of contrast. (b) shows the zoom-in view of the dark region in (a). (c) shows the crystal lattice mostly of the lighter Cu-rich phase.

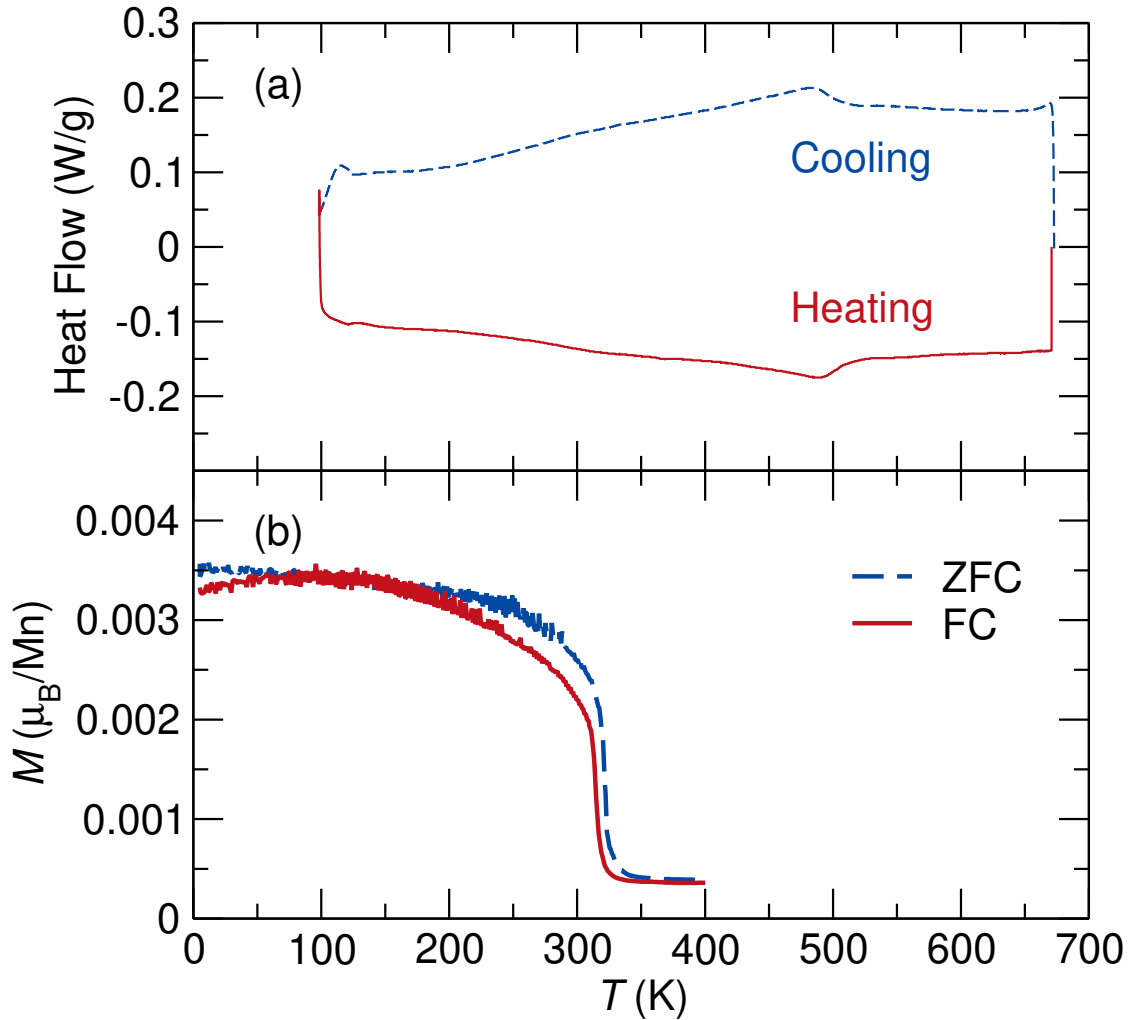


Figure 4: Near-stoichiometric $\text{CuMn}_{0.964}\text{As}_{1.036}$ DSC data in (a) and field cooling and zero field cooling magnetization in (b) show two transitions in the near-stoichiometric sample at around 315 K and 490 K. The transition at 490 K corresponds to the T_N , while an uncompensated moment develops at 315 K due to a transition to weak ferromagnetism (canting) or subtle phase separation.

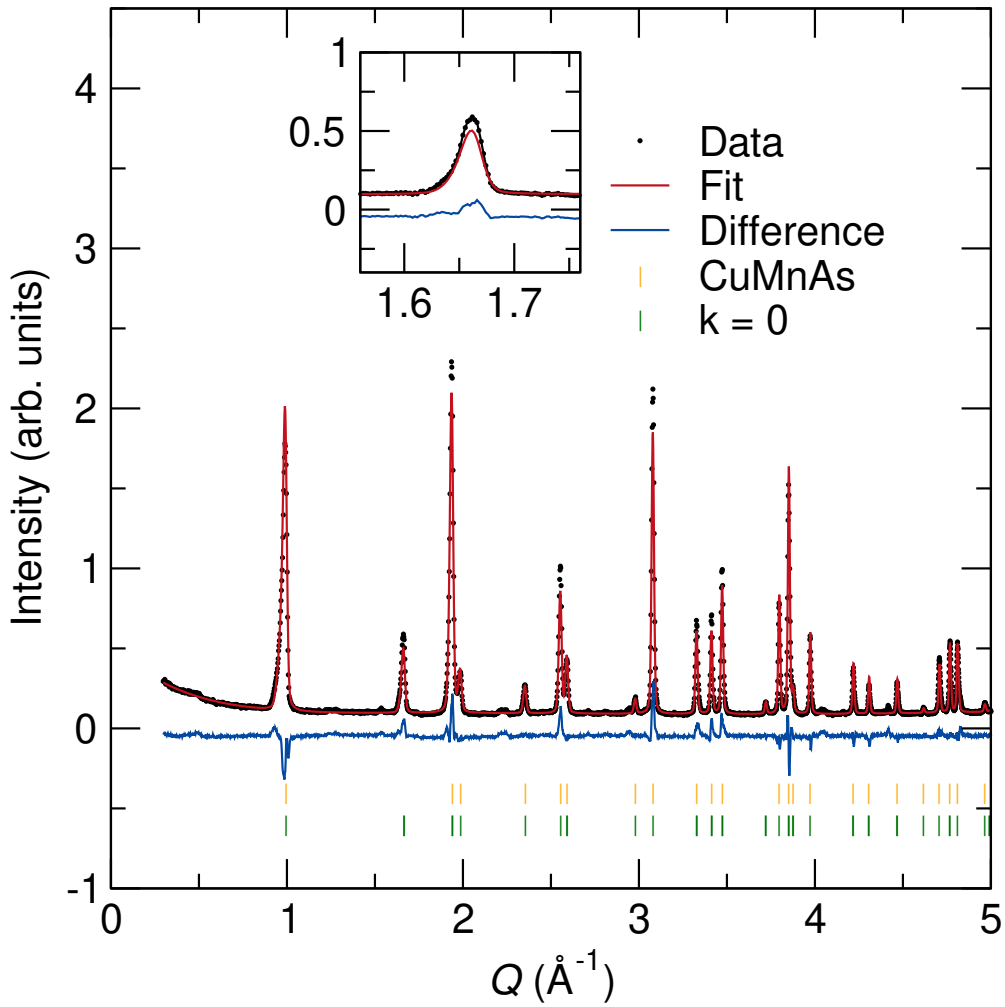


Figure 5: Rietveld fit to Echidna NPD data of the near-stoichiometric sample $\text{CuMn}_{0.964}\text{As}_{1.036}$ at 4 K confirms the $Pm'mn$ magnetic space group. The magnetic moment on Mn sites is refined to be $3.73(3)\ \mu_B$.

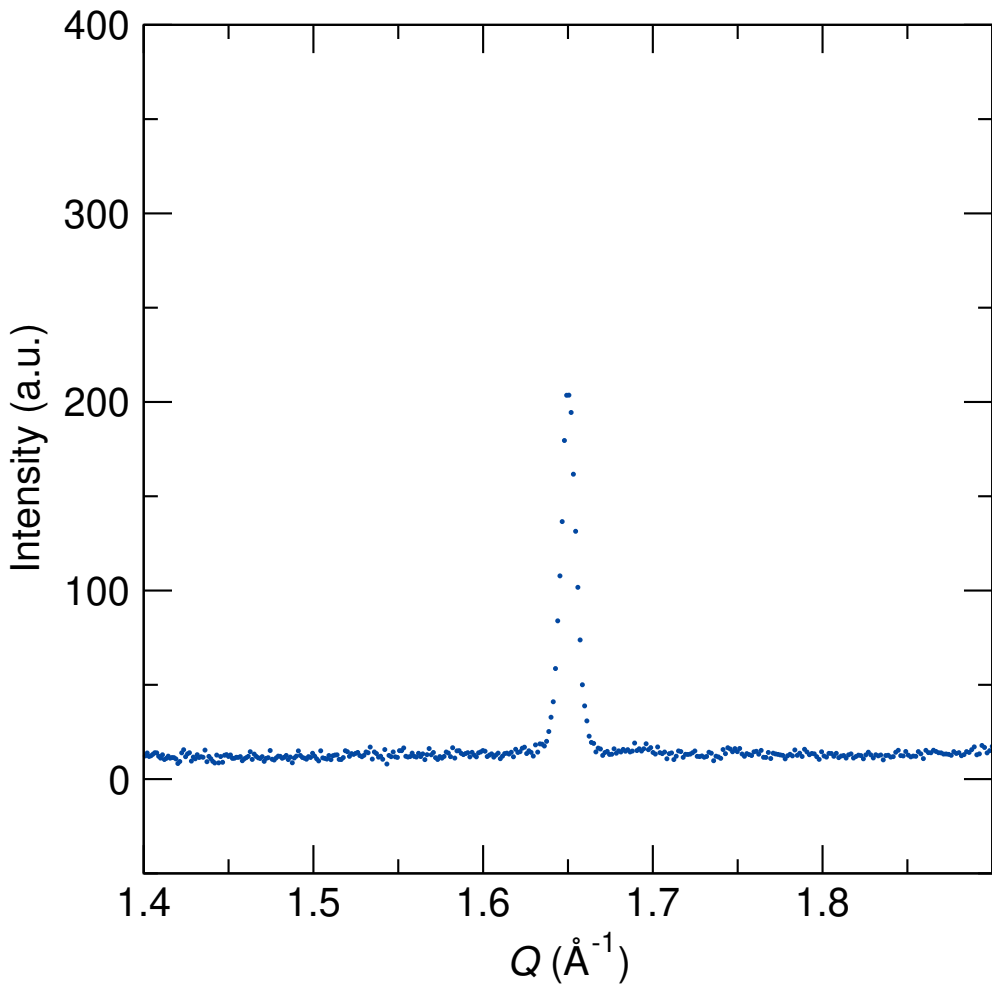


Figure 6: 300 K POWGEN NPD data showing the presence of the 100 magnetic peak in $\text{Cu}_{1.18}\text{Mn}_{0.82}\text{As}$.

Table 1: Spacegroups corresponding to the k-maximal subgroups for $P4/nmm1'$ space group and $k = 0$ propagation vector.

No.	Group symbol
1	$P4/n'm'm'$
2	$P4'/n'mm'$
3	$P4/nm'm'$
4	$P4'/n'm'm$
5	$P4'/nmm'$
6	$P4'/nm'm$
7	$P4/n'mm$
8	$P4/nmm$
9	$Cmm'a'$
10	$Cm'ma$
11	$Pmm'n'$
12	$Pm'mn$

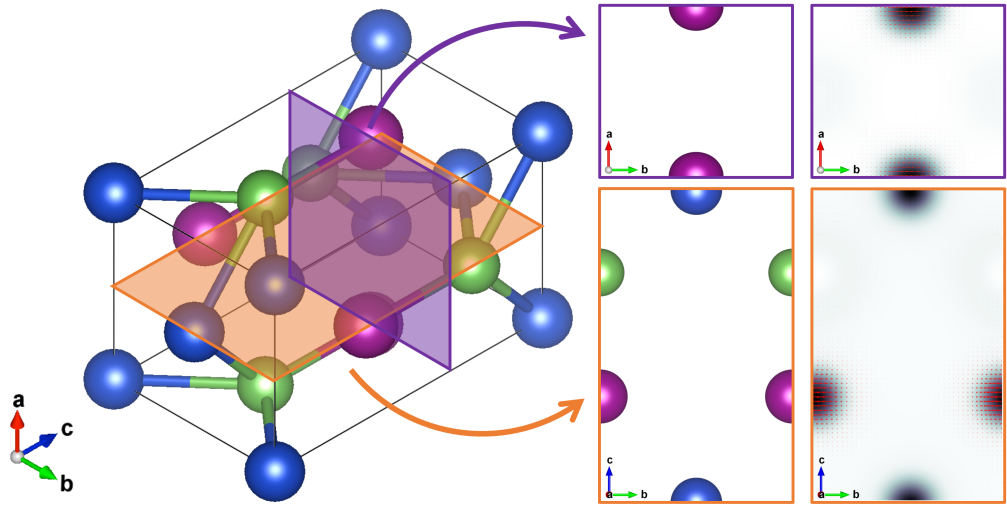


Figure 7: The DFT calculated electron charge (Grayscale) and magnetization densities (Red vectors) of tetragonal CuMnAs in ab -plane at $z = 0.657$ (Purple boxes) and bc -plane at $a = 0.500$. Color contrast and vector size presents the relative density change. Blue, purple, and green spheres represent the element of Cu, Mn, and As, respectively.

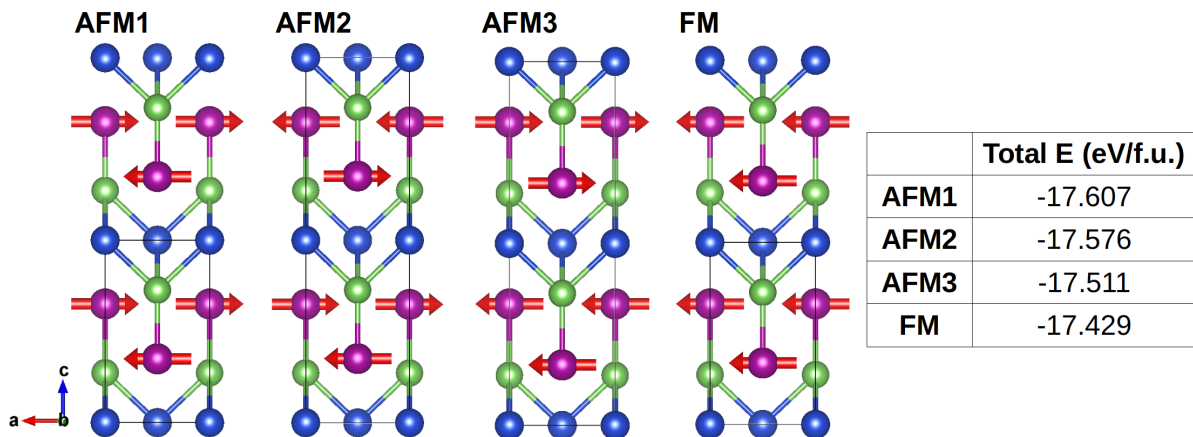


Figure 8: Three antiferromagnetic (AFM) configurations and one ferromagnetic (FM) configuration with DFT total energies tabulated for comparison. AFM1 is the ground state structure of CuMnAs which has the lowest total energy per formula unit (f.u.). Solid gray lines show the magnetic unit cells.

Sequential peak fits shown in Fig. 2(b) and S1 was performed using GSAS-II. The c lattice parameter was extracted by fitting of a pseudo Voigt peak to the 001 reflection in the dataset and results are shown in the tables below. In case of the POWGEN NPD data, the peak position, intensity, Gaussian and Lorentzian peak width parameters for the 001 peak were allowed to refine. For the 11-BM XRD peak fit data in Fig. 2 (b), the Gaussian peak width parameter for the 001 peak was fixed to the instrumental parameters and the other three parameters were allowed to refine. For the Wombat peak fit data in S1, a simple Gaussian peak fitting was done with the Lorentzian peak fit parameters fixed to 0. For all the sequential peak fits, a third order Chebychev polynomial was used to fit the background and the refined values were allowed to copy from one temperature data to the next sequentially. Fig. S9 shows the fit to the 001 peak of the 152 K $\text{Cu}_{1.18}\text{Mn}_{0.82}\text{As}$ sample measured at POWGEN. Tables S2, S3 and S4 show the refined peak fitting parameters corresponding to the POWGEN NPD, 11-BM XRD and Wombat NPD data of $\text{Cu}_{1.18}\text{Mn}_{0.82}\text{As}$ respectively.

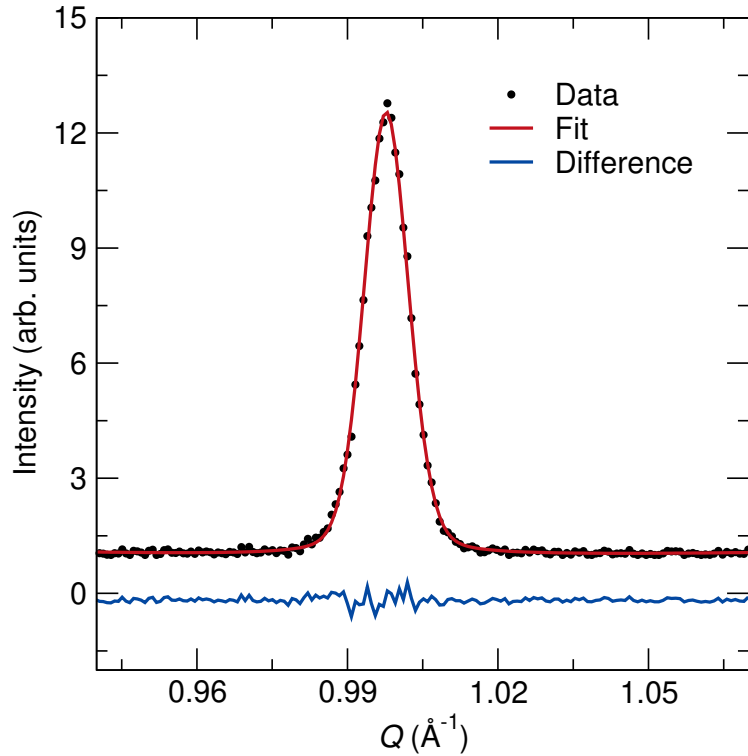


Figure 9: The peak fit to the 001 peak of the POWGEN NPD data at 152 K.

Table 2: Refined sequential peak fitting parameters to the 001 reflection along with their standard deviations for the POWGEN Cu-excess Cu_{0.82}Mn_{1.18}As NPD data shown in Fig. 2(b).

temp	Rwp	pos0	esd-pos0	int0	esd-int0	sig0	esd-sig0	gam0	esd-gam0
498.697	19.70919995	142064.2043	11.89517485	91.03075408	3.172722017	261111.8668	32730.36639	289.631438	94.00402322
492.118	13.54110369	142022.9316	8.376332891	92.26197397	2.116154708	293682.0572	23720.95443	278.9033833	64.26491834
482.03	15.09778924	142022.1066	9.23202068	92.01398648	2.3077987	263327.9765	25164.49605	340.1299723	69.54713756
472.059	12.5558187	142029.2615	8.039087335	91.68728784	1.969934601	288853.4697	23499.52459	356.1407048	62.45386417
462.058	13.69273752	142036.5159	8.632418293	89.81623427	2.120571812	306329.7096	25264.35808	277.7943791	67.54215898
452.059	14.52488361	142042.0642	9.242748057	89.11976022	2.245279882	295945.1682	26812.1146	307.1378455	72.00291804
442.058	13.14758744	142052.7763	8.201075086	92.25994085	2.053191097	278420.1242	22979.57566	320.5502855	62.66029647
432.058	13.39151292	142089.467	8.593366857	100.2217677	2.197344135	266209.2117	23967.23283	423.0849619	63.81899171
422.058	13.63456674	142121.7202	8.64524663	102.4950383	2.309466379	288728.6549	24664.71592	348.9224182	65.36248483
412.063	12.08780665	142135.8681	7.570366948	107.0243996	2.152104344	311238.6256	22055.32004	295.6162067	57.91037431
402.108	12.56172878	142163.1174	7.953752978	115.1970066	2.2512583	276751.3963	21929.95057	402.6866303	57.03588341
392.056	11.80367431	142182.2056	7.406429919	115.0788471	2.191776553	311919.9111	21252.28163	308.1759318	55.13847276
382.077	11.9935159	142183.1995	7.362049041	120.4085156	2.262025715	302706.2256	20646.3983	310.8026878	53.78951368
371.751	10.41975736	142205.2772	6.392465754	120.9675868	1.891036256	280899.1454	17141.77449	364.0328098	44.63232954
363.362	12.91860046	142194.8479	7.853146669	126.1723885	2.442981183	260486.7334	20534.89779	393.8394959	54.26538639
350.794	11.83335286	142215.4703	7.412986512	131.8806781	2.423036751	308390.7117	20865.67004	335.7074678	53.23594496
341.971	10.22148203	142222.2726	6.269498476	134.1329972	2.10031602	3128882.699	17599.88764	304.1651145	45.05911
332.061	10.52695386	142224.9366	6.499426145	136.3004857	2.171009655	303511.2201	18194.88143	352.6541033	46.1689538
322.066	10.92999646	142211.0947	6.614516374	139.224979	2.204126961	280621.325	17356.75226	356.6054537	44.7361311
312.074	10.36017591	142198.564	6.37019055	140.9445976	2.154896862	286832.7771	17229.70134	380.6751165	44.00912864
302.082	9.596990264	142195.3467	5.785224313	143.2223686	2.071439294	296868.5662	15770.61611	322.8685853	41.04099938
292.069	9.521755809	142180.7335	5.709152175	144.1244066	2.04792454	311356.9425	15656.4054	280.2254865	40.19971928
282.063	10.37817594	142174.5027	6.227032556	150.9172264	2.241212811	267834.4901	16321.75197	390.0768859	42.15654282
272.056	9.273976232	142157.6046	5.564263522	152.5458677	2.060504925	317670.4759	15069.96668	291.6131932	38.16997117
261.993	8.436090716	142139.5171	5.07537608	153.3416852	1.840642791	283253.4929	13273.47396	357.7666187	33.99971475
251.985	9.11517559	142123.862	5.454546747	154.7994422	2.012814595	292723.8553	14330.05008	330.4267415	36.69104893
242	7.817654705	142102.9272	4.805040842	157.5478564	1.841567223	323867.5524	13503.86984	308.2787958	33.79148516
232.01	8.347922128	142094.1284	5.043567996	162.8928885	1.908216283	271400.0774	13045.40672	396.8823716	33.24305185
222.015	7.819109279	142073.7458	4.75904787	160.7743943	1.851393515	327412.2318	13250.91091	290.4404306	33.15431454
212.028	8.17778606	142066.3556	4.837631829	159.0741978	1.849344885	301349.4494	12613.1721	293.627302	32.34942052
202.024	8.228743731	142057.2846	5.005763881	165.8895115	1.993152128	306187.1818	13640.77823	339.802775	34.4648655
192.026	8.415283195	142032.9036	5.066331911	167.6992859	1.97476538	298696.9035	13333.91623	343.5551142	33.51005934
182.047	7.463744237	142024.8804	4.460787198	164.9643845	1.766085965	316943.9959	11990.59891	284.6743197	30.2655757
172.058	7.800704689	142013.178	4.617229936	167.4163055	1.848451317	307473.1461	12162.58332	292.5265345	30.88205289
162.08	8.482397174	141993.9853	5.096087829	173.8399244	2.087653031	289897.1563	13490.2768	362.0933478	34.18123743
152.068	7.823312938	141986.611	4.691766772	174.3034442	1.920973621	311738.9485	12527.16636	311.8343925	31.35023139
143.277	9.620936814	141967.474	5.807960476	178.0064684	2.44214405	306679.0547	15577.52104	340.1741943	39.07347679

Table 3: Refined sequential peak fitting parameters to the 001 reflection along with their standard deviations for the 11-BM Cu-excess Cu_{0.82}Mn_{1.18}As XRD data shown in Fig. 2(b).

temp	Rwp	pos0	esd-pos0	int0	esd-int0	gam0	esd-gam0
100	15.40898477	3.764751113	8.35E-05	33397.07756	382.2453044	1.056735425	0.0212632189557216
105.2	17.51546945	3.764491436	0.000104633	34843.33894	452.9700072	1.22996291	0.0273718893032842
110.2	16.64001045	3.764090143	9.31E-05	36398.23524	438.1340359	1.152604608	0.0242939727914342
115.2	16.08480568	3.763800051	8.10E-05	40066.97151	449.0246268	1.028639678	0.0204436614313128
120.2	16.51867079	3.763768404	8.33E-05	43355.88086	491.7798408	1.057780746	0.0210815150360724
125.19	15.59653616	3.763375851	7.96E-05	43692.66835	466.142366	1.08234984	0.0201860482607935
130.19	16.28443385	3.763254547	8.20E-05	42699.49297	475.9167351	1.050960312	0.020656638909363
135.19	15.99554012	3.762955582	8.21E-05	39542.65787	444.2611975	1.051928087	0.020853206888371
140.2	15.65893372	3.76270489	7.93E-05	40360.71056	437.8302686	1.050677538	0.0200367693083477
145.27	15.62411654	3.76268682	7.99E-05	38887.88471	425.2170108	1.045245065	0.0201324794950738
150.15	15.81089208	3.762378479	8.27E-05	36948.46815	415.6468142	1.06638088	0.0210261887152205
155.17	15.62338487	3.762268703	8.01E-05	36358.49056	405.1793984	1.029045531	0.0204203609270273
160.21	15.45819148	3.762137295	7.82E-05	36624.75282	401.3950352	1.01860072	0.019818137325659
165.2	15.81840785	3.76182039	8.20E-05	35941.4254	406.7087208	1.052284262	0.0209886756959273
170.19	15.29252082	3.761747786	7.91E-05	36207.27257	395.007062	1.043800044	0.0201340126245682
175.2	15.24794647	3.761338738	7.73E-05	35582.816	386.2799501	1.015979053	0.019655253890676
180.2	16.15203071	3.761274717	8.07E-05	35760.24772	410.4768422	0.995531207	0.020433692799927
185.21	15.36129759	3.76115447	7.82E-05	35568.75545	391.3019804	1.020036428	0.0198986975224395
190.19	15.13780374	3.761107791	7.76E-05	36015.07521	387.9481262	1.035911341	0.0197357621932927
195.19	15.08483973	3.760780175	7.64E-05	35995.75982	386.4955387	1.008597481	0.0191879155602154
200.2	14.96575267	3.760576062	7.63E-05	36070.41271	384.1977905	1.02802052	0.0193391758595985
205.19	15.15841732	3.760436746	7.74E-05	35999.53596	387.4603528	1.030211139	0.0196103502064985
210.18	14.9717003	3.760286392	7.63E-05	34973.29904	375.8489549	1.011371857	0.0193170880132166
215.13	14.91454304	3.760012086	7.59E-05	35195.77941	377.0560308	1.0075744	0.019098232808584
220.17	15.89122801	3.760077826	8.03E-05	35285.51522	399.7829089	1.006310965	0.0203254030717933
225.16	15.27657253	3.759864671	7.72E-05	35932.01875	389.6442907	1.012736164	0.0194062512326813
230.15	14.90683396	3.759650396	7.54E-05	35793.32411	379.2563944	1.014432984	0.0190559684970362
235.16	15.28680237	3.759591037	7.86E-05	35097.45213	385.5297731	1.017278298	0.0197364155761368
240.14	15.06844322	3.759502947	7.75E-05	35512.11483	379.6821172	1.041441279	0.0195960612897471
245.13	15.57641979	3.759513688	7.91E-05	34863.22697	388.8833498	0.99873588	0.0198386838705586
250.12	15.35333721	3.759542482	7.90E-05	35367.9909	387.9153201	1.028026098	0.0198406781274231
255.09	15.72595555	3.759588805	7.88E-05	35225.98073	392.3778012	0.991575466	0.019635686402649
260.1	15.55673461	3.759555153	7.86E-05	35277.69165	390.6356289	1.001028798	0.0195966164539501
265.08	15.63534499	3.759596244	7.85E-05	35062.66853	391.9005865	0.992035516	0.0197869791847228
270.09	15.95765712	3.759389735	8.00E-05	35234.57073	401.9811962	0.990931752	0.0200992258818481
275.11	15.42941352	3.759290621	7.65E-05	35201.4097	386.9702441	0.974941054	0.0191008186566161
280.1	15.16564964	3.759033566	7.61E-05	35656.53038	383.1062221	1.001045446	0.0189728894043922
285.11	15.67590988	3.758862529	7.93E-05	35225.51762	394.0171707	1.007101466	0.019969634736104
290.12	15.25928936	3.758650651	7.69E-05	34518.50687	378.6811582	0.984482722	0.0191758043680333
295.09	14.84767236	3.758528724	7.53E-05	35119.78487	371.6292695	1.008052226	0.0187802482874206
300.15	15.24209309	3.758358833	7.57E-05	34298.3956	374.8426533	0.963329949	0.0187970868737863

305.09	14.79775567	3.758172646	7.24E-05	35226.25348	368.8454206	0.960666297	0.0178306333997266
310.12	14.3282203	3.758110765	7.05E-05	35756.39404	361.7063091	0.976204573	0.0175457230138955
315.83	13.85510229	3.757953688	6.70E-05	36180.04514	350.8458103	0.955159639	0.0164512960163215
320.02	11.37940007	3.758176236	5.16E-05	37681.50513	291.4604792	0.892724354	0.0123091897394304
325.2	11.17482615	3.758132607	4.71E-05	38691.74526	287.4427031	0.824236423	0.0111072794521553
329.9	10.33446143	3.758297639	4.16E-05	38868.44885	263.8618366	0.768996066	0.00954610950563794
334.96	9.956208556	3.758436172	3.89E-05	39164.77307	254.2327092	0.734596084	0.00877774699703509
340.25	9.403174501	3.75858751	3.53E-05	40110.94539	242.5647047	0.702700273	0.00789560242962205
345.27	9.76542834	3.758552612	3.54E-05	40128.74931	251.1607097	0.657928367	0.00777902094197381
350.23	9.840460907	3.758665684	3.51E-05	40266.36631	252.7593054	0.6441682	0.00769741474775996
355.38	10.3248673	3.758876461	3.69E-05	40047.20736	264.8910918	0.641257556	0.00803429397476061
360.33	10.1947289	3.759016254	3.56E-05	40124.10888	261.6940894	0.617763071	0.00773605736756989
365.26	10.51603188	3.759369846	3.63E-05	43080.01186	283.7433985	0.624634581	0.00784401144994696
370.01	10.79352108	3.759564117	3.71E-05	43019.45781	291.1149261	0.616661036	0.00797155134049598
375.1	10.27845062	3.759835284	3.55E-05	43039.78161	277.0625168	0.623949946	0.00766775822245959
380.12	11.12539058	3.760080812	3.76E-05	42642.05213	296.98925	0.596441441	0.00802700976218355
385.3	10.54782969	3.760511148	3.54E-05	44358.55929	289.8647602	0.598951931	0.00754289577463892
389.97	10.7942556	3.760867239	3.57E-05	45656.56665	302.4390332	0.591327851	0.00753935412423171
394.96	10.65902673	3.761224217	3.57E-05	46444.08129	303.4439861	0.605295357	0.00757227221748354
399.96	9.695928737	3.761745525	3.25E-05	46470.25039	275.6935058	0.612042346	0.00696908292538409
405	10.84712877	3.761917685	3.73E-05	46589.59889	310.5796502	0.630435007	0.0079598784973985
410.13	11.44325611	3.762422128	4.03E-05	46185.21545	326.1164035	0.652977742	0.00864539826926886
414.99	11.63158536	3.762842638	4.16E-05	45638.00518	328.6148828	0.665555947	0.00890745305045242
420.15	11.16260733	3.763367875	4.03E-05	45392.87451	314.2806841	0.673528959	0.00864243855463501
425.14	11.33650796	3.763681376	4.01E-05	45231.48778	317.557912	0.654379643	0.00861016789831714
430.17	10.64769826	3.764006894	3.65E-05	44311.49973	292.9864259	0.619244665	0.00783234922720501
435.25	10.4220952	3.764322265	3.43E-05	44086.44815	284.964483	0.580715505	0.00737227895145399
440.14	10.10917038	3.764435604	3.21E-05	43825.11119	273.1317943	0.552451109	0.00685338475593841
445.26	9.462606348	3.764537493	2.91E-05	43876.79674	255.894621	0.523602011	0.00621245579953472
450.32	9.054984747	3.76462077	2.72E-05	43587.34706	243.3447585	0.501106865	0.00577838893756978
455.37	10.19865966	3.76465697	3.00E-05	43584.72908	272.8056885	0.483380883	0.00632642902762149
460.46	9.539136882	3.764881769	2.74E-05	43348.93234	254.0139352	0.462112587	0.00580362841825301
465.13	8.538396941	3.764687691	2.40E-05	43008.46016	224.9367321	0.444243371	0.00504165114184438
470.33	8.95335558	3.764662579	2.51E-05	42978.81798	235.9361856	0.443117583	0.00529368839531341
475.34	8.864990657	3.764586369	2.48E-05	42525.91916	231.4459592	0.441554305	0.00523668190338918
480.23	9.684587259	3.764558131	2.75E-05	41553.38031	249.6543345	0.445155289	0.00581408325888385

Table 4: Refined sequential peak fitting parameters to the 001 reflection along with their standard deviations for the Wombat Cu_{0.82}Mn_{1.18}As XRD data shown in Fig. S1.

temp	Rwp	pos0	esd-pos0	int0	esd-int0	sig0	esd-sig0
15.0093	2.854853291	21.92272617	0.004092967	380177.2816	3876.632204	1409.892651	37.9223619662951
20.0055	2.889402599	21.92123854	0.004129074	381807.8208	3929.75035	1405.989165	38.1920813416562
25.0033	2.850599506	21.91809677	0.004037098	381601.0628	3847.207311	1372.241621	36.7900558642892
29.9996	3.194539358	21.91540408	0.004524125	382981.1402	4326.544183	1380.85982	41.4444304570222
34.9858	3.1083564	21.91464761	0.004369889	385468.9417	4203.044569	1367.812042	39.7623053238669
39.972	3.020827136	21.91679919	0.004235903	384742.7602	4077.768833	1351.633511	38.3198098787686
45.0021	2.962663943	21.91407696	0.004158933	382627.4128	3987.397808	1334.758365	37.2713868867435
50.1008	2.918840446	21.91435206	0.004105848	384063.2479	3945.416869	1346.718126	37.0960468741626
55.1986	3.05890192	21.91660673	0.004283034	385362.1142	4132.191503	1347.319177	38.7453434406783
60.3007	3.200020699	21.91492761	0.004484061	384148.0091	4312.150144	1350.808372	40.5409139636033
65.353	3.104185628	21.91540753	0.00436497	382671.3568	4179.189	1353.0041	39.5071947240561
70.3992	3.047770618	21.91329811	0.0042774	383771.4632	4102.610743	1355.768487	38.71621404171
75.4216	3.240342504	21.91210335	0.004543773	381964.8237	4347.690581	1342.040941	40.9331065639604
80.4594	3.029876405	21.91383898	0.00424803	381918.1549	4068.220181	1330.987252	38.1283675839476
85.4615	2.906157849	21.91103928	0.004103658	382756.1692	3921.372877	1365.127178	37.3697206375552
90.4671	2.960410939	21.91211798	0.004159066	382229.6195	3973.106021	1353.047069	37.5725594541275
95.4614	3.084925431	21.91201565	0.004333198	379858.0393	4126.284513	1336.187812	38.9965119258992
100.464	3.224865575	21.91060705	0.004538936	379571.9389	4319.643771	1337.93226	40.8362187651514
105.466	3.154655005	21.9085769	0.004416421	381270.7463	4215.504609	1339.337345	39.7134783122608
110.458	3.123204383	21.91015931	0.00438404	380006.5094	4177.221012	1333.233224	39.3947902233174
115.46	3.086357193	21.90904737	0.004287301	381487.0689	4111.556366	1306.201356	38.0018443443138
120.453	3.03169838	21.90847347	0.004254293	380606.0891	4060.333125	1331.33731	38.1069568155862
125.45	2.904302228	21.9082303	0.004077323	381516.8913	3903.344892	1328.62168	36.5127003250654
130.395	3.113396674	21.90653373	0.004397682	379739.2838	4183.643499	1341.631819	39.6955642777154
135.4	2.979391498	21.90657787	0.004218195	379314.4581	4013.664378	1338.385134	38.0252225833893
140.407	3.011572733	21.90496695	0.004260674	379305.9327	4053.408699	1333.934024	38.1862056077721
145.398	2.903480603	21.90254707	0.004098893	378639.6734	3893.61042	1328.294297	36.67425980905
150.391	3.141144859	21.90347539	0.004440743	378642.7398	4221.752343	1331.676068	39.9608650356348
155.392	2.947179396	21.90243155	0.004199122	376880.9393	3964.852598	1353.048038	38.1170827821062
160.385	2.741308279	21.90353151	0.003910623	374622.8352	3670.242136	1351.985801	35.3736275985411
165.388	3.045980775	21.89915048	0.004347885	374560.0467	4080.241446	1354.798398	39.4989194639846
170.382	3.004675556	21.90028009	0.004290812	373055.1217	4013.773015	1344.883798	38.8708868389681
175.384	3.099432953	21.89627003	0.004411228	373647.584	4138.081573	1341.17985	39.8573728820509
180.379	3.025372645	21.89597268	0.004324805	369870.3355	4021.921602	1330.271517	38.8691079541265
185.379	3.022287339	21.89537552	0.004310161	370571.2935	4018.425894	1326.509137	38.5856969323809
190.371	2.957882457	21.89319274	0.004257737	366598.8348	3924.826009	1336.077939	38.3130631936896
195.371	2.666134883	21.89339164	0.003826681	367572.9857	3536.584169	1331.551327	34.3568228131088
200.363	3.022331187	21.8917403	0.004344816	367046.5398	4008.148832	1340.053967	39.2581934774517
205.365	2.942678471	21.88945652	0.004228598	365653.0863	3889.088912	1328.763045	37.8456451765898
210.359	3.142429282	21.88730028	0.004511471	362669.5099	4128.455997	1312.839229	40.2281212042576
215.356	2.759341036	21.88779157	0.003992372	362922.1378	3642.037114	1334.617528	35.8856186500462

220.347	2.910806245	21.88348019	0.004222324	359455.6963	3822.910119	1328.112706	37.8814569908907
225.338	3.085798411	21.88207963	0.004481339	358701.1932	4048.054899	1334.852229	40.3722782204839
230.337	2.88395726	21.88295219	0.004216967	357947.3247	3795.19877	1343.809583	38.1173580792114
235.33	2.929767064	21.88156014	0.004258298	355854.7966	3825.723507	1318.417643	38.0861008092353
240.329	2.92741548	21.87885815	0.004275616	353332.4292	3814.423094	1320.265108	38.3253702059497
245.321	2.899819226	21.87562074	0.004240178	351243.4548	3763.899416	1312.270088	37.8440356334742
250.323	2.862217096	21.87589249	0.004203781	350170.8836	3719.287212	1321.09425	37.6203412904972
255.316	2.745286936	21.87731852	0.004075167	348099.3341	3574.846609	1347.133903	36.9380093944504
260.316	2.939230927	21.87400092	0.004345696	346630.8144	3804.11437	1326.941593	39.001908826738
265.312	2.754428728	21.87259949	0.004059079	345371.888	3543.638049	1316.721865	36.2840881912612
270.311	2.754933586	21.87319899	0.004092339	342521.4845	3542.856953	1319.886353	36.6347300042819
275.302	2.724900267	21.87006678	0.004054851	338628.1274	3480.411953	1308.378449	36.1480581901135
280.303	2.680131804	21.86707639	0.003997963	338329.6423	3429.523831	1309.846211	35.6528476792393
285.293	2.803512333	21.86638335	0.004198631	335154.4011	3573.197126	1307.710865	37.4860682994106
290.292	2.479133314	21.86410866	0.003734317	332770.9736	3155.090642	1304.847259	33.2061367396018
295.283	2.734869094	21.86076684	0.004130657	333300.5115	3488.431956	1325.469799	37.1813905946469
300.283	2.731745932	21.86018328	0.004134237	331006.5159	3470.276173	1321.77425	37.1392923400313

Table 5: Rietveld refinement parameters for the room temperature 11-BM XRD data of Cu_{1.18}Mn_{0.82}As sample shown in Fig. 1(a). The figures of merit are wR = 20.34%, chi² = 119544, GOF = 2.19.

names	Scale	DisplaceX	DisplaceY					
values	6.6110	-79.4442	1029.7001					
sig	0.0224	2.9959	28.2396					
names	bg1	bg2	bg3	bg4	bg5	bg6	bg7	bg8
values	40.06	-59.41	-34.54	921.1	533.6	-4216	-1416	8130
sig	0.2233	1.401	3.767	13.55	14.18	35.74	10.72	16.14
names	bg9	bg10	bg11	bg12				
values	1229	-6971	-305.4	2187				
sig	15.62	40.03	16.09	32.68				
	CuMnAs							
names	a	b	c	Volume	Size	Mustrain		
values	3.799452	3.799452	6.297675	90.912	0.66317	2884.1		
sig	0.000051	0.000051	0.000083	0.003	0.0355	32.2		
name	x	y	z	frac	Uiso			
As1								
values	0.25000	0.25000	0.23702	1.000	0.00583			
sig			0.00023		0.00041			
Cu1								
values	-0.25000	0.25000	0.50000	1.000	0.00864			
sig					0.00033			
Mn1								
values	0.25	0.25	-0.16672	0.820	0.01901			
sig			0.00029	0.00	0.00072			
Cu2								
values	0.25	0.25	-0.16672	0.180	0.01901			
sig			0.00029	0.00	0.00072			

Table 6: Rietveld refinement parameters for the 500 K Cu_{1.18}Mn_{0.82}As POWGEN NPD data shown in Fig. 1(b). The figures of merit are wR = 8.83%, chi² = 43085.9, GOF = 3.66. The sum of the phase fractions of the two phases was constrained to be 1. The following atoms were constrained to be equivalent - CuMnAs:Mn1 = CuMnAs:Cu2.

names	Scale	Zero	difA	difB	difC		
values	26472.4699	43.497655	4.050819	-19.982011	22542.803876		
sig	124.0812	3.016729	0.426505	1.301858	2.116480		
names	X Y Z						
values	-16.761112	2.851714	11.524797				
sig	0.891635	6.706909	1.281101				
names	bg1	bg2	bg3	bg4	bg5		
values	12.12	-1.67	-7.61	23.96	12.67		
sig	0.2251	0.636	1.621	2.313	1.96		
	bg6						
	CuMnAs						
names	a	b	c	Volume	Size	Mustain	Phase fraction
values	3.831959	3.831959	6.293129	92.408	0.98788	990.4	0.98988
sig	0.000111	0.000111	0.000173	0.008	2.8909	39.8	0.00063
name	x	y	z	frac	Uiso		
As1							
values	0.25000	0.25000	0.23671	1.000	0.01261		
sig			0.00027		0.00038		
Cu1							
values	-0.25000	0.25000	0.50000	1.000	0.01783		
sig					0.00025		
Mn1							
values	0.25000	0.25000	-0.17123	0.813	0.00916		
sig			0.00097	0.004	0.00134		
Cu2							
values	0.25000	0.25000	-0.17123	0.187	0.00916		
sig			0.00097	0.004	0.00134		
	MnO						
names	a	b	c	Volume	Size	Mustain	Phase fraction
values	4.452986	4.452986	4.452986	88.299	1.0	1159.5	0.01012
sig	0.000490	0.000490	0.000490	0.029		417.6	0.00063
name	x	y	z	frac	Uiso		
Mn1							
values	0.00000	0.00000	0.00000	1.000	0.00781		

sig	
O1	
values	0.50000 0.50000 0.50000 1.000 0.00912
sig	

Table 7: Rietveld refinement parameters for the 500 K Cu_{0.64}Mn_{1.36}As POWGEN NPD data shown in Fig. 5. The figures of merit are wR = 8.55%, chi² = 44425.8, GOF = 3.68. The sum of all the structural phases were constrained to be 1. The following atoms were constrained to be equivalent - CuMnAs-1:Cu1 = CuMnAs-1:Mn2, CuMnAs-2:Mn1 = CuMnAs-2:Cu4 = k=[001/2]:Mn1_0, CuMnAs-2:Mn2 = CuMnAs-2:Cu5 = k=[001/2]:Mn2_1. Crystallite size, mustrain and lattice parameters of CuMnAs-2 and k=[001/2] were constrained to be equal.

names	Scale	Absorption					
values	23483.6778	0.0148					
sig	359.7159	0.0022					
names	bg1	bg2	bg3	bg4	bg5	bg6	
values	18.04	0.3393	-12.76	14.14	13.25	-19.38	
sig	0.2421	0.6309	1.797	2.335	2.147	2.355	
	CuMnAs-1						
names	a	b	c	Volume	Size	Mustrain	Phase fraction
values	3.850603	3.850603	6.317257	93.667	2.65410	3135.4	0.69521
sig	0.000098	0.000098	0.000213	0.004	2.9726	75.5	0.00514
name	x	y	z	frac	Uiso		
As1							
values	0.25000	0.25000	0.24283	1.000	0.01236		
sig			0.00059		0.00071		
Cu1							
values	-0.25000	0.25000	0.50000	0.795	0.01537		
sig				0.006	0.00096		
Mn1							
values	0.25000	0.25000	-0.16616	1.000	0.02033		
sig			0.00099		0.00126		
Mn2							
values	-0.25000	0.25000	0.50000	0.205	0.01537		
sig				0.006	0.00096		
	CuMnAs-2						
names	a	b	c	Volume	Size	Mustrain	Phase fraction
values	3.80904	3.80904	6.30661	91.501	0.38432	2623.2	0.28625
sig					0.1298	151.3	0.00744
names	D11	D33					
values	2.076e-06	-3.62e-06					
sig	5.472e-06	2.155e-06					
name	x	y	z	frac	Uiso		

As1 values	0.25000	0.25000	0.73340	1.000	0.01089		
sig			0.00137		0.00175		
Mn1 values	0.75000	0.25000	0.00000	0.957	0.00291		
sig				0.041	0.00365		
Mn2 values	0.25000	0.25000	0.32696	0.954	0.00863		
sig			0.00223	0.046	0.00453		
Cu4 values	0.75000	0.25000	0.00000	0.043	0.00291		
sig				0.041	0.00365		
Cu5 values	0.25000	0.25000	0.32696	0.046	0.00863		
sig			0.00223	0.046	0.00453		
<hr/>							
k = [001/2]							
names	a	b	c	Volume	Size	Mustrain	Phase fraction
values	3.80904	3.80904	12.61323	183.003	0.38432	2623.2	0.14312
sig					0.1298	151.3	0.00372
<hr/>							
names	D11	D22	D33				
values	2.076e-06	2.076e-06	-3.62e-06				
sig	5.472e-06	5.472e-06	2.155e-06				
<hr/>							
name	x	y	z	frac	Uiiso		
Mn1_0 values	0.25000	0.75000	0.00000	0.957	0.00291		
sig				0.041	0.00365		
Mn2_1 values	0.75000	0.75000	0.16348	0.954	0.00863		
sig			0.00112	0.046	0.00453		
<hr/>							
name	My						
Mn1_0 values	0.946						
sig	0.094						
Mn2_1 values	-2.872						
sig	0.138						
<hr/>							
MnO							
names	a	b	c	Volume	Size	Mustrain	Phase fraction

values	4.453855	4.453855	4.453855	88.350	1.0	2943.8	0.01854
sig	0.000650	0.000650	0.000650	0.039		274.4	0.00248
<hr/>							
name	x	y	z	frac	Uiso		
Mn1							
values	0.00000	0.00000	0.00000	1.000	0.00781		
sig							
O1							
values	0.50000	0.50000	0.50000	1.000	0.00912		
sig							

Table 8: Rietveld refinement parameters for the 300 K Cu_{0.64}Mn_{1.36}As POWGEN NPD data shown in Fig. 6. The figures of merit are wR = 9.24%, chi² = 66237.2, GOF = 4.55. The sum of all the structural phases were constrained to be 1. The following atoms were constrained to be equivalent - CuMnAs-1:Cu1 = CuMnAs-1:Mn2, CuMnAs-1:Mn1 = k=0:Mn1_1, CuMnAs-2:Mn1 = CuMnAs-2:Cu4 = k=[001/2]:Mn1_0, CuMnAs-2:Mn2 = CuMnAs-2:Cu5 = k=[001/2]:Mn2_1. Crystallite size, mustrain and lattice parameters of CuMnAs-1 and k=0, CuMnAs-2 and k=[001/2] were constrained to be equal.

names	Scale	Absorption				
values	32640.2847	0.0472				
sig	2534.3204	0.0027				
names	bg1	bg2	bg3	bg4	bg5	bg6
values	13.91	-2.752	5.464	35.19	-1.032	-38.96
sig	0.2748	0.6991	2.05	2.724	2.409	2.72
	CuMnAs-1					
names	a	b	c	Volume	Size	Mustrain
values	3.79264	3.79264	6.32209	90.938	0.31072	2909.0
sig					0.0426	75.0
	CuMnAs-2					
names	D11	D33				
values	4.924e-05	2.853e-06				
sig	3.366e-06	1.56e-06				
name	x	y	z	frac	Uiso	
As1						
values	0.25000	0.25000	0.24027	1.000	0.01168	
sig			0.00054		0.00082	
Cu1						
values	-0.25000	0.25000	0.50000	0.809	0.01214	
sig				0.010	0.00095	
Mn1						
values	0.25000	0.25000	-0.16436	1.000	0.01580	
sig			0.00094		0.00105	
Mn2						
values	-0.25000	0.25000	0.50000	0.191	0.01214	
sig				0.010	0.00095	
	CuMnAs-2					
names	a	b	c	Volume	Size	Mustrain
values	3.78586	3.78586	6.29098	90.167	0.49549	2575.7
sig					0.2355	169.7
						0.04327

names	D11	D33					
values	-9.187e-05	-9.262e-06					
sig	7.711e-06	1.688e-06					
name	x	y	z	frac	Uiiso		
As1							
values	0.25000	0.25000	0.73333	0.808	0.00451		
sig			0.00170	0.087	0.00311		
Mn1							
values	0.75000	0.25000	0.00000	0.986	0.00368		
sig				0.073	0.00341		
Mn2							
values	0.25000	0.25000	0.32711	0.958	0.01515		
sig			0.00330	0.121	0.00434		
Cu4							
values	0.75000	0.25000	0.00000	0.014	0.00368		
sig				0.073	0.00341		
Cu5							
values	0.25000	0.25000	0.32711	0.042	0.01515		
sig			0.00330	0.121	0.00434		
	$k = [001/2]$						
names	a	b	c	Volume	Size	Mustrain	Phase fraction
values	3.78586	3.78586	12.58195	180.334	0.49549	2575.7	0.14222
sig					0.2355	169.7	0.02163
name	D11	D22	D33				
values	-9.187e-05	-9.187e-05	-9.262e-06				
sig	7.711e-06	7.711e-06	1.688e-06				
name	x	y	z	frac	Uiiso		
Mn1_0							
values	0.25000	0.75000	0.00000	0.986	0.00368		
sig				0.073	0.00341		
Mn2_1							
values	0.75000	0.75000	0.15647	0.958	0.01515		
sig			0.00661	0.121	0.00434		
name	My						
Mn1_0							
values	1.382						
sig	0.112						
Mn2_1							

values	-3.876						
sig	0.369						
$k = 0$							
names	a	b	c	Volume	Size	Mustrain	Phase fraction
values	3.79264	3.79264	6.32209	90.938	0.31072	2909.0	0.70386
sig					0.0426	75.0	0.06387
names	D11	D22	D33				
values	4.924e-05	4.924e-05	2.853e-06				
sig	3.366e-06	3.366e-06	1.56e-06				
name	x	y	z	frac	Uiiso		
Mn1_1							
values	0.25000	0.25000	0.83564	1.000	0.01580		
sig			0.00094		0.00105		
name	Mx						
Mn1_1							
values	3.066						
sig	0.069						
MnO							
names	a	b	c	Volume	Size	Mustrain	Phase fraction
values	4.441468	4.441468	4.441468	87.615	1.0	2326.9	0.01170
sig	0.000855	0.000855	0.000855	0.051		350.8	0.02062
name	x	y	z	frac	Uiiso		
Mn1							
values	0.00000	0.00000	0.00000	1.000	0.00781		
sig							
O1							
values	0.50000	0.50000	0.50000	1.000	0.00912		
sig							

Table 9: Rietveld refinement parameters for the room temperature CuMn_{0.964}As_{1.036} lab-source XRD data shown in Fig. 7(a). The figures of merit are wR = 4.72%, chi² = 286935, GOF = 8.43.

names	Scale	Shift	Transparency				
values	959.1755	34.7276	3.1775				
sig	7.1741	1.9226	0.1837				
names	bg1	bg2	bg3	bg4	bg5	bg6	
values	2.74e+04	66.33	8533	1.425e+04	-4.734e+04	-1.628e+04	
sig	58.52	268.4	1122	1910	5432	3944	
names	bg7	bg8	bg9				
values	8.393e+04	2340	-4.369e+04				
sig	9029	2406	4789				
CuMnAs							
names	a	b	c	Volume	Size	Mustrain	March-Dollase
values	3.798740	3.798740	6.342385	91.523	0.13017	567.7	0.8171
sig	0.000114	0.000114	0.000178	0.008	0.0040	95.8	0.0022
name	x	y	z	frac	Uiso		
As1							
values	0.25000	0.25000	0.22954	1.000	0.01837		
sig			0.00047		0.00123		
Cu1							
values	-0.25000	0.25000	0.50000	1.000	0.02533		
sig					0.00104		
Mn1							
values	0.25000	0.25000	-0.16357	1.000	0.05016		
sig			0.00076		0.00244		

Table 10: Rietveld refinement parameters for the 520 K CuMn_{0.964}As_{1.036} Echidna NPD data shown in Fig. 7(b). The figures of merit are wR = 6.05%, chi² = 17600.9, GOF = 2.41. The atomic fractions were constrained to be 1 for all atoms. The crystallite size, mustrain and the lattice parameters were constrained to be equal between the CuMnAs and k=0 phase. CuMnAs:Mn1 was constrained to be equivalent to k=0:Mn1_1.

names	Scale	DisplaceX	DisplaceY			
values	170953.6042	143.2791	-719.8432			
sig	1052.1409	17.1238	19.7740			
names	bg1	bg2	bg3	bg4	bg5	bg6
values	1131	-71.04	235.2	-119.9	849.7	1710
sig	4.257	18.84	82.01	142.5	408.4	305.3
names	bg7	bg8	bg9			
values	-3244	-2454	3549			
sig	696.3	191.9	377.7			
CuMnAs						
names	a	b	c	Volume	Size	Mustrain
values	3.83151	3.83151	6.33953	93.067	1.0	2004.2
sig						36.4
names	D11	D33				
values	-2.391e-06	-2.623e-07				
sig	2.663e-06	1.445e-06				
name	x	y	z	frac	Uiso	
As1						
values	0.25000	0.25000	0.23741	1.000	0.01193	
sig			0.00046		0.00133	
Cu1						
values	-0.25000	0.25000	0.50000	1.000	0.02023	
sig					0.00060	
Mn1						
values	0.25000	0.25000	-0.16787	1.000	0.03952	
sig			0.00096		0.00238	
<i>k</i> = 0						
names	a	b	c	Volume	Size	Mustrain
values	3.83151	3.83151	6.33953	93.067	1.0	2004.2
sig						36.4
names	D11	D22	D33			

values	-2.391e-06	-2.391e-06	-2.623e-07		
sig	2.663e-06	2.663e-06	1.445e-06		
name	x	y	z	frac	Uiso
Mn1_1					
values	0.25000	0.25000	0.83213	1.000	0.03952
sig			0.00096		0.00238
name	Mx				
Mn1_1					
values	1.478				
sig	0.042				

Table 11: Rietveld refinement parameters for the 4 K CuMn_{0.964}As_{1.036} Echidna NPD data shown in Fig. S5. The figures of merit are wR = 8.80%, chi² = 35035.9, GOF = 3.35. The atomic fractions were constrained to be 1 for all atoms. The crystallite size, mustrain and the lattice parameters were constrained to be equal between the CuMnAs and k=0 phase. The isotropic thermal parameters were set to 0.0001.

names	Scale	DisplaceX	DisplaceY			
values	182925.5424	73.5671	-702.8654			
sig	932.2109	17.6553	20.2704			
names	bg1	bg2	bg3	bg4	bg5	bg6
values	892.9	-25.66	197.5	-198.1	886.2	1708
sig	5.593	24.25	107.9	189.4	549.7	418.6
names	bg7	bg8	bg9			
values	-3577	-2252	3695			
sig	963.5	272	539.1			
	CuMnAs					
names	a	b	c	Volume	Size	Mustrain
values	3.77883	3.77883	6.33191	90.417	1.0	2375.8
sig						36.5
names	D11	D33				
values	-1.655e-06	1.152e-06				
sig	2.762e-06	1.476e-06				
name	x	y	z	frac	Uiso	
As1						
values	0.25000	0.25000	0.23435	1.000	0.00010	
sig			0.00038			
Cu1						
values	-0.25000	0.25000	0.50000	1.000	0.00010	
sig						
Mn1						
values	0.25000	0.25000	-0.16259	1.000	0.00010	
sig			0.00079			
	<i>k</i> = 0					
names	a	b	c	Volume	Size	Mustrain
values	3.77883	3.77883	6.33191	90.417	1.0	2375.8
sig						36.5
names	D11	D22	D33			

values	-1.655e-06	-1.655e-06	1.152e-06		
sig	2.762e-06	2.762e-06	1.476e-06		
name	x	y	z	frac	Uiso
Mn1_1					
values	0.25000	0.75000	0.83741	1.000	0.00010
sig			0.00079		
name	My				
Mn1_1					
values	3.733				
sig	0.029				